Computational and Experimental Comparison of the Effects of Porosity on the Piezoelectric Characteristics of Polyvinylidene Fluoride (PVDF) Thin Films

A Thesis

SUBMITTED TO THE FACULTY OF THE UNIVERSITY OF MINNESOTA DULUTH

BY

Jack T. Kloster

IN PARTIAL FULFILLMENT OF THE REQUIREMENTS FOR THE DEGREE OF MASTER OF SCIENCE

Advisor:

Ping Zhao, Ph.D.

June 2022

Jack T. Kloster

Acknowledgements

I would like to offer special thanks to my advisor, Dr. Ping Zhao, as well as Dr. Victor Lai, who both guided me in my research and were always available to answer questions and provide invaluable feedback.

I would also like to thank Dr. Michael Pluimer. Without his recommendation of the Applied Materials Science program, I would have likely never pursued my master's degree.

I would like to thank my fellow master's students of Applied Materials Science, Ty Lindley, Mark Iwen, Nicole Franklin, and Ryan Marhula. The mutual support we all provided not only made graduate school endurable, but enjoyable.

Lastly, I want to show my appreciation for the students who partnered with me in this research: Matt Danley, to whom I could always complain about troubleshooting issues that would magically fix themselves; Stephen (Zhaolin) Gao, who taught me how to synthesize PVDF; and Tony Struntz, who took on the burden of PVDF synthesis when I needed it most. I couldn't have done it without you all.

Abstract

Polyvinylidene Fluoride (PVDF) is a piezoelectric polymer that is uniquely suited for biosensing applications due to its biocompatibility, sensitivity to changes in pressure, and simplicity to fabricate. PVDF thin films have shown potential in the application of hemodynamic flow sensing and monitoring the effects on blood flow caused by prosthetic valve implantation via the transcatheter aortic valve replacement (TAVR) operation. The piezoelectric performance of PVDF films can be influenced by the porosity of the material. In this study, strain tracking was performed on thin film PVDF specimens with various levels of porosity and pore sizes to determine the mechanical properties of the specimens. The mechanical properties were used to model the PVDF material in COMSOL Multiphysics software, in which compression and tensile test simulations were performed to determine the piezoelectric coefficients of the PVDF. Experimental compression tests were performed so that the results could be compared with the simulated results. The simulated results were also compared with experimental results achieved from a previous study through tensile testing of PVDF. Simulated results showed that piezoelectric performance of PVDF increased as porosity increased, and specimens with the smallest pore sizes exhibited the highest performance. Piezoelectric coefficients d_{33} and d_{31} ranged from 4.8-16.9 pC/N and 16.4-47.2 pC/N, respectively, which resemble the expected values based on literature. Experimental tensile test results closely resembled the simulated results. However, experimental compression tests showed insignificant change in the piezoelectric performance of PVDF as the porosity of the material increased.

Table of Contents

List of Figures

Chapter 1: Introduction

Polyvinylidene fluoride (PVDF) is a piezoelectric polymer material that has shown great aptitude as a pressure sensor, especially in biomedical applications. By enhancing the piezoelectric characteristics of PVDF, the material can be improved to be a more sensitive, consistent, and robust sensor, suited for a wide variety of applications. One potential application for PVDF sensors is for monitoring hemodynamic flow during in vitro studies of blood flow in the aorta after implantation of a prosthetic valve via the transcatheter aortic valve replacement (TAVR) operation. There are numerous periprocedural complications that are associated with the TAVR operation; monitoring how the procedure affects blood flow has the potential to lead to technological advancements that could greatly improve patient outcomes. This study investigates methods for enhancing the piezoelectric properties of PVDF.

1.1 Transcatheter Aortic Valve Replacement (TAVR)

In recent years, the TAVR operation has become an increasingly common procedure for replacing the aortic valves in the hearts of patients suffering from aortic valve stenosis. Figure 1 illustrates the prosthetic valve deployment process in three steps. The TAVR procedure has been lauded as a minimally invasive alternative to the conventional surgical aortic valve replacement (SAVR) procedure. The operation is especially popular for patients who are deemed intermediate-to-high risk and would otherwise be ineligible for a valve replacement surgery. Unfortunately, the TAVR operation does not come without its share of periprocedural complications. A 2012 study[1] examined the morbidities and mortality outcomes following the TAVR procedure, including the 30-day mortality (8.5%), 1-year mortality (22.8%), 2-year mortality

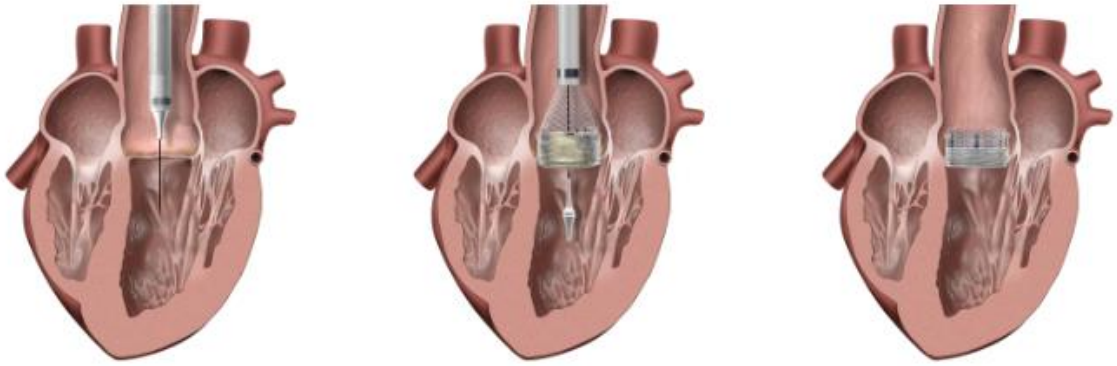

Figure 1. Illustration of the TAVR procedure in three steps[4]

(26.5%), and the 30-day stroke (2.6%). Other post-procedure complications included major vascular complication (6.6%), cardiac tamponade (1.4%), aortic dissection (0.71%), aortic rupture (0.49%), coronary obstruction (0.72%), myocardial infarction (0.56%), valve embolization (0.56%), paravalvular aortic regurgitation (11.6%), and endocarditis (0.39%). Another study examined how the evolution from the first generation of prosthetic valves to the second generation affected the rates of periprocedural complications[2]. Advances in the TAVR procedure and valve design have been able to significantly reduce the rates of many TAVR-related complications, such as paravalvular leakage (12.39% to 1.75%), stroke (2.79% to 2.09%), myocardial infarction (1.39% to 0.45%), coronary obstruction (0.99% to 0.13%), vascular complication (11.51% to 5.42%), bleeding (9.27% to 7.48%), and mortality (5.41% to 1.47%). These improvements in periprocedural complications can be attributed to an increase in operator experience and advances in prosthetic valve design, notably in that second-generation valves are able to be repositioned or retrieved post-implantation, whereas first generation valves, if defective or mispositioned, required an additional prosthesis to be

implemented[3]. Additionally, complication rates have been reduced due to patient samples, as lower risk patients have become a larger proportion of TAVR subjects[2].

These advances in operator experience and prosthetic valve technology, and the effect they have had on reducing negative outcomes for patients, have proven extremely beneficial for the post-procedure outlook of TAVR. However, there is still opportunity for further advancement in improving the TAVR procedure, valve technology, and making the operation safer for patients overall. Development of repeatable bench-top tests for studying how prosthetic valve implantation affects blood flow, as well as how the artificial valve interacts with the structure of the heart, could lead to invaluable research and development of improved procedures and technologies for TAVR operations. Potential advancements could lead to further reduction in periprocedural complications, making the TAVR procedure an increasingly safe and suitable option for lower-risk patients.

1.2 Hemodynamic and Cardiological Sensors

To perform in vitro testing of a TAVR procedure, an appropriate sensor must be selected for monitoring hemodynamic conditions and various kinetic forces throughout the artificial heart model. A relevant experiment performed in 2018 by Hatoum et al.[5] studied the effects of two types of artificial aortic valves (self-expandable and balloon-expandable) on the hemodynamics within a rigid, cylindrical valve chamber, as well as a realistic aorta model with calcified leaflets. This realistic aorta model was based on the CT scans of a real patient's heart. To monitor the hemodynamic conditions within the heart models, the study utilized particle image velocimetry (PIV) to track the velocities of fluorescent micro-scale particles which were mixed with the test fluid. Using the PIV

method, the conditions measured included the transvalvular pressure gradient, vorticity, Reynolds shear stress, and turbulent kinetic energy. From these factors, the study determined that the valves were able to create a more ideal seal in the cylindrical valve chamber model due to its circular cross section geometry. In the patient-specific aorta model, the balloon-expandable valve was able to produce lower pressure gradients due to the radial force that the balloon generated during deployment. Figure 2 displays the turbulent kinetic energy (TKE) in the patient-specific model as measured by PIV. It shows TKE during acceleration, systolic, deceleration, and diastolic stages of flow, and the TKE gradient is measured based on the velocities of the fluorescent particles in the fluid.

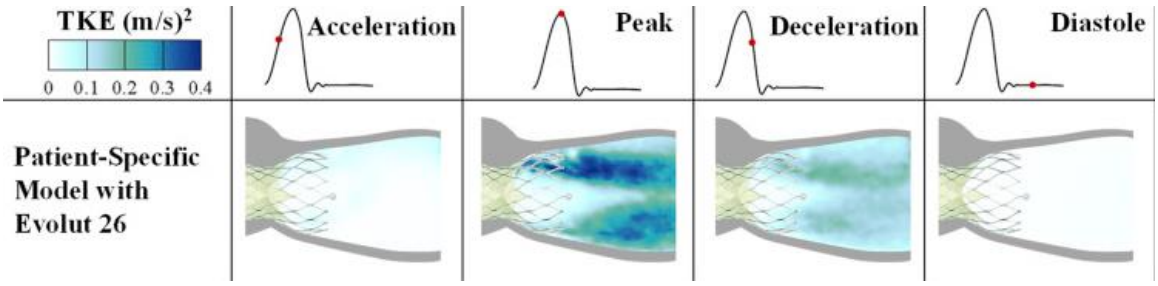

Figure 2. Turbulent kinetic energy (TKE) in a patient-specific aorta model, as measured by PIV[5]

Another method for monitoring cardiological conditions is by measuring intrathoracic impedance. A diagnostic device was developed by Medtronic in 2005 which was able to measure the impedance across a standard defibrillator coil[6]. The impedance across the device would increase in the presence of accumulating pulmonary fluid, a portent of heart failure, and would alert patients and physicians of the increasing danger.

Piezoelectric sensors are commonly used for measuring pressure, and examples of such devices can be found in the field of hemodynamic monitoring. In 2005, Medtronic

developed an implantable hemodynamic monitor device, named Chronicle, that utilized the piezoelectric effect to measure systolic, diastolic, and pulse pressures in the right ventricle[7]. The device was also capable of estimating the pulmonary arterial diastolic pressure, as well as measuring the pre-ejection interval and systolic time interval. The sensor within the device consisted of a titanium diaphragm which would deflect under changing pressures in the surrounding environment. Upon deflection of the diaphragm, its capacitance would be altered, signifying the magnitude of the pressure change. The device was determined to be a safe and effective way for monitoring hemodynamics within the hearts of patients. Unfortunately, the Chronicle device failed to receive approval from the FDA in 2007 due to its inability to improve clinical outcomes in patients[8].

The CardioMEMS device, developed by Abbott Laboratories, used a similar micro-electromechanical systems (MEMS) technology to monitor pulmonary arterial pressure[9]. The device used a pressure-sensitive capacitor, sandwiched between fused silica, which was coupled with the electronics in the device electromagnetically by induction through a coil[10]. The implanted CardioMEMS device, by relaying to physicians valuable information about pressures in the pulmonary artery, was able to help guide heart failure treatment and was found to reduce patient hospitalization for heart failure by as much as 48%[9]. These results show that MEMS are highly capable and effective in the application of hemodynamic sensory and monitoring, and show great potential for improving patient outcomes by providing crucial information about conditions that are known to portend heart failure.

1.3 Piezoelectric Sensors

Piezoelectric materials are a unique branch of materials, often used in MEMS, that are capable of generating electric potentials when subjected to mechanical stress. This ability to transduce kinetic energy into an electrical signal makes piezoelectric materials uniquely suited for use in pressure sensory and related applications. The mechanism that allows for this phenomenon to occur is the molecular polarization of the material's crystalline structure[11]. Mechanical loads on the material cause physical displacements in the crystal lattice, which lead to a displacement of the material's dielectric poles, known as a charge separation. As the charge separation changes under dynamic loading, so does the electric potential between the opposite surfaces of the piezoelectric material. With the use of electrodes applied to opposite surfaces, the changes in electric potential can be measured and used to determine the mechanical stress within the material. This principle is known as the direct piezoelectric effect, and it can also be applied conversely (called the inverse piezoelectric effect) by subjecting the material to an electric field and inducing mechanical stresses within the material. Since a piezoelectric material is, by definition, electrically polarized, the piezoelectric coefficient, d, is a naturally anisotropic material property, meaning the d coefficient is unique depending on the direction of mechanical loading. The most common directions of interest, regarding the piezoelectric coefficient, are d_{33} (where the electrode is applied to the X-Y face and the load is applied in the Z direction) and d_{31} (where the electrode is applied to the X-Y face and the load is applied in the Y direction). The d_{33} and d_{31} modes are illustrated in Figure 3.

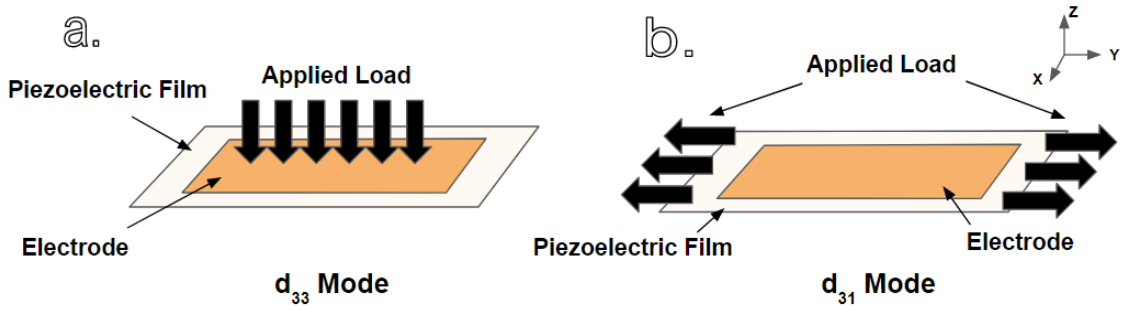

Figure 3: Loading conditions for d_{33} (a) and d_{31} modes (b)

There are a variety of piezoelectric materials in existence, both naturally forming and synthetic. Piezoelectric materials can come in the form of crystals, such as quartz, berlinite, tourmaline, and Rochelle salt[12]; ceramics, such as barium titanate and lead zirconate titanate (PZT)[13]; and polymers, such as polyamides, polylactic acids, and (most notably) polyvinylidene fluoride (PVDF)[12]. These materials are used for a wide variety of sensing applications. Quartz crystals have been used for applications ranging from accelerometers[13] to immunosensors, capable of detecting reactions between antigens and antibodies by measuring variances in crystal oscillation rates[12]. Piezoceramics like PZT have been used as knock sensors in automobiles, as well as acoustic sensors, such as ultrasound transducers and sonar sensors[13]. PZT and PVDF are the most common examples of piezoelectric materials being used in the application of flow sensors[14], the most relevant application when considering hemodynamics.

1.4 PVDF Applications

PVDF has a history of being used in various biomedical applications as a pressure and flow sensor. Sharma et al. has shown in multiple publications that PVDF as a thin film can be used as a pressure sensor integrated with a catheter for measuring intravascular forces during surgery[15]. In a 2003 study, a PVDF thin film material was developed for monitoring cardiorespiratory conditions during sleep for patients with

cardiorespiratory sleep disorders[16]. The sensor device could be placed under the patient and measure the forces caused by heartbeats and diaphragm movement during sleep to monitor health. This technology was further developed by Choi et al. in 2006 when they integrated the PVDF film sensor in a wearable belt device[17].

In application as a flow sensor, PVDF has been developed for measuring flow rates and pressures of both liquids and gases alike, proving that it is a material capable of consistently generating electric signals proportional to the surrounding pressure[18], while remaining robust, compact, and relatively simple to produce[19]. PVDF has also served in the biomedical industry as a flow sensor for measuring the flow rate of blood in the portal vein during liver transplant surgery[20]. Patients who suffer from liver cirrhosis often develop portosystemic shunts that divert blood flow away from the portal vein due to hypertension in the liver. Upon receiving a new liver, this reduced blood flow may lead to continued liver damage. Alternatively, if the patient receives a partial liver, an overflow of blood can similarly cause damage. Therefore, it is crucial to monitor and control the flow of blood through the portal vein in patients undergoing liver transplant surgery. Previously, portal vein blood flow was measured using ultrasound technology, which is a method highly dependent on operator expertise and experience. Another monitoring method used involved a thermal sensor located on the end of a catheter. Cold saline solution was mixed with the blood, and the temperature sensor could determine the flow rate based on the rate of temperature change and the concentration of saline solution in the patient's blood. However, this method made continuous monitoring impractical since the concentration of saline in the blood was unsustainable[20]. As an alternative solution for monitoring blood flow in the portal vein, a spirally wound PVDF thin film

was developed to be implanted in the vein (illustrated in Figure 4). The PVDF sensor was determined to effectively measure flow rate with a sensitivity of 0.02 mV peak-to-peak per 20 ml/min over a range of flow rates from 600 to 1800 ml/min. The sensor's measurements were also determined to be stable over a duration of 120 minutes[20]. Blood flow rate across the aortic valve is typically much greater than in the portal vein, at approximately 12,000 ml/min[21] and 662 ml/min[22], respectively. However, blood velocities in the two regions are on a similar scale, ranging from 11 to 66 cm/sec in the aorta[23] and 20 to 40 cm/sec in the portal vein[24].

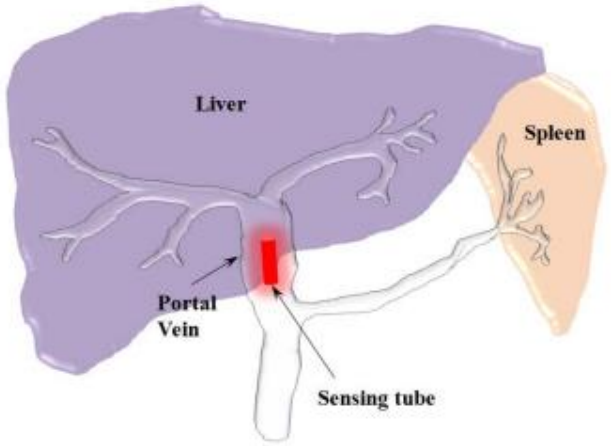

Figure 4: Illustration of the PVDF tube sensor implanted in the portal vein[20]

Therefore, a similar PVDF flow sensor could potentially be scaled and developed for use in the aortic valve. PVDF is uniquely suited for biomedical applications due to its biological inertness, ability to generate relatively large voltage signals under a wide range of stresses, compactness as a thin film, and flexibility[14]. Furthermore, PVDF has the benefit of generating its own electricity when sensing pressures, and thus no battery or other power source is required for the sensor.

1.5 PVDF Characterization

The PVDF polymer structure is made up primarily of three different copolymers, referred to as alpha (α), beta (β), and gamma (γ) phases, as shown in Figure 5. The α-phase of PVDF is the most stable of the conformations and typically the most dominant in the polymer structure immediately after synthesis. However, the α-phase does not exhibit a dipole, and thus does not contribute to the piezoelectric characteristics of the material[25]. The β-phase exhibits the greatest dipole of the conformations and is thus most associated with the piezoelectric properties of PVDF. The γ-phase is similarly polar. However, it typically makes up a much smaller portion of the overall structure, giving it a smaller influence on the material's properties.

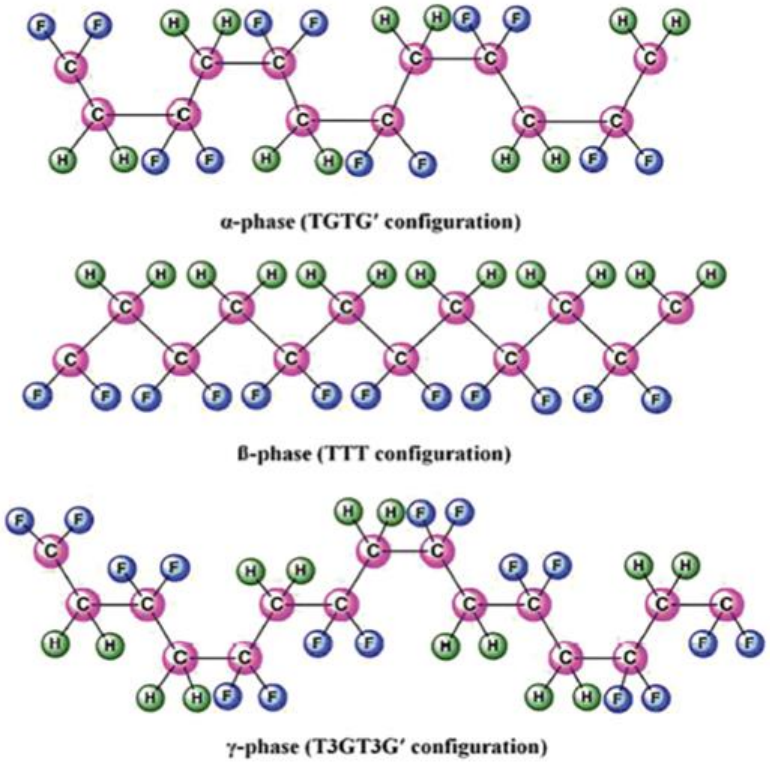

Figure 5. The three main conformations of PVDF, α-, β-, and γ-phases[26]

There exist a few common methods used for increasing the concentration of β-phase within PVDF. Mechanical stretching on the material can result in increased alignment of the amorphous regions in the polymer, and can also lead to transformation from α-phase to β-phase, improving the piezoelectric characteristics. Electric poling is another method for improving β-phase concentrations. By applying high voltages across the material, nonpolar conformations can be transformed into the polar β-phase. Additionally, both the stretching and poling methods can benefit from being performed in conjunction with thermal annealing, which acts to increase the conformations' susceptibility to transformation[25].

β-phase formation in PVDF has also been shown to be influenced by conditions during its synthesis. Chinaglia et al. showed that the solvent evaporation rate during solution casting of PVDF can greatly influence the presence of β-phase within the polymer[27]. PVDF solutions that were cast at lower temperatures were found to exhibit slower solvent evaporation rates and significantly larger concentrations of β-phase, approaching nearly 100% β-phase when the dimethylformamide (DMF) solvent was evaporated at 60 °C. In a 2008 study[28], various solvents were used for solution casting of PVDF, and the effects of their evaporation rates on the formation of β-phase were studied. It was determined that solvents with higher boiling points exhibited slower evaporation rates, and thus led to the formation of more β-phase under identical temperature conditions. The study also found that β-phase was the primary conformation formed at evaporation rates lower than 4.1 mg/min, and that above that rate α-phase began to form in higher concentrations, resulting in muted piezoelectric properties.

Therefore, solvent evaporation rate is a crucial factor to control during synthesis of PVDF via solution casting since it can greatly affect the piezoelectric properties of the material.

Porosity has become a factor of great interest with respect to the piezoelectric performance of PVDF. Increasing the number and size of pores within the material can increase the mechanical strain under identical loading conditions. This increased strain leads to larger charge separations at the molecular level, resulting in greater electric polarization and improved overall piezoelectric performance[29]. There are multiple methods for introducing porosity in PVDF films during synthesis. One method is by mixing solvents. The mixed-solvents method is founded on the principle that two mixed solvents will have different evaporation rates. As one solvent evaporates more rapidly, the surface tension will begin to change, and water droplets will form on the surface of the PVDF film. As these water droplets evaporate, pores in the surface of the material will be left in their place. By mixing acetone and methyl ethyl-ketone (MEK, also referred to as 2-butanone), this method of introducing pores in PVDF has been shown to improve piezoelectric performance by as much as 107%[29].

Another method for introducing void regions in PVDF is by integrating pore-inducing particles in the polymer solution during the solution casting process[30]. A 2014 study[31] utilized this method for introducing pores into PVDF thin films. During the synthesis process, zinc-oxide (ZnO) nanoparticles were added to the PVDF solution before solution casting. Once the films were cast, they were bathed in hydrochloric acid (HCl), which dissolved the ZnO particles, leaving behind nano-scale pores in their place. This process is illustrated in Figure 6. PVDF specimens were synthesized with various ZnO mass fractions, ranging from 10% to 70% ZnO as a fraction of total mass before

etching. The greatest piezoelectric performance was exhibited at a removed ZnO mass fraction of 50%. At higher mass fractions of ZnO, the voltage signals generated by the PVDF films began to decrease, likely due to the overall reduction of PVDF material in the films[31]. From these results, it is clear that the piezoelectric performance of PVDF thin films can greatly benefit from the introduction of pores within the material's structure. This enhancement in performance has potential to improve PVDF's candidacy for pressure sensing applications in the biomedical industry, specifically for monitoring hemodynamic flow within the aortic valve. Advancing this sensory technology could lead to further developing valve prosthesis technology, which could reduce TAVR-related complications and further mitigate negative patient outcomes.

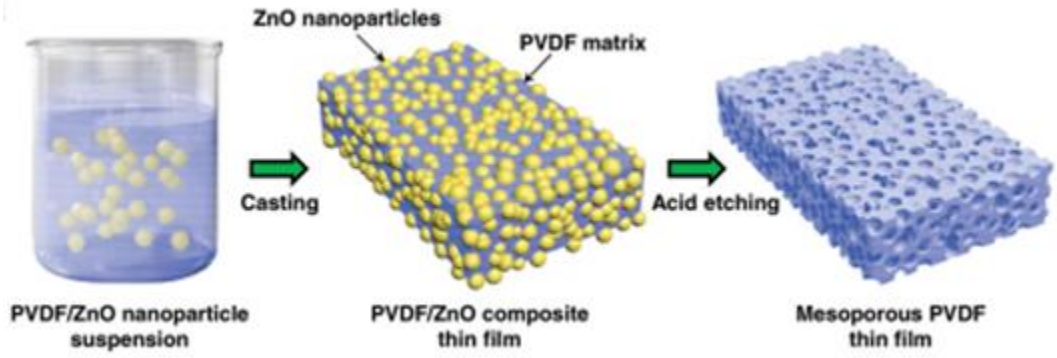

Figure 6: Illustration of porosity being introduced via ZnO etching[31]

1.6 Experiment and Motivation

The goal of this study is to further investigate the piezoelectric performance of PVDF thin films, especially how performance is affected by the introduction of porosity via ZnO etching. PVDF specimens, synthesized using the solution casting method, are tested under compressive stresses to determine their piezoelectric coefficient, d_{33}. Various mass fractions and sizes of ZnO nanoparticles are used to induce a variety of pore volumes and sizes. Furthermore, visual strain tracking software is utilized to determine

mechanical properties of the PVDF, and these mechanical properties are used to model a simulated PVDF material so experimental tests can be replicated by finite element analysis (FEA) simulations. These simulated results of the piezoelectric properties serve to further validate the experimental results. By investigating the piezoelectric properties of PVDF and the effect porosity has on its electromechanical performance, there is potential for further development of PVDF as a hemodynamic sensor that can lead to further technological advancements in the biomedical field, benefiting patients and physicians alike.

Chapter 2: Materials and Methods

2.1 PVDF Synthesis and Preparation

PVDF samples were synthesized using the solvent casting method. PVDF powder (Sigma Aldrich) was placed in a vial and dissolved in 15 mL of 2-butanone (methyl-ethyl ketone) (Sigma Aldrich). To expedite the dissolution of PVDF, the solution was placed in an oven at 80 ºC. The vial was intermittently (approximately once per minute) removed from the oven and shaken by hand to prevent the precipitation of solid PVDF at the bottom of the vial. After approximately 15 minutes in the oven, the PVDF solution turned from opaque to transparent, indicating that the PVDF had fully dissolved in the 2-butanone, at which point the solution was removed from the oven and the ZnO particles (US Research Nanomaterials Inc.) were added to the solution. In the case of pure PVDF specimens, the solution was poured directly into Petri dishes (without the addition of any ZnO particles) which were placed back in the oven at 80 ºC for solvent casting. PVDF-ZnO specimens had ZnO added to the solution to meet the desired mass fraction. Specimens were made with a mix of PVDF-ZnO that ranged from 0-50% ZnO by mass, in increments of 10%. The sum of the masses of PVDF and ZnO in the solution was always measured to be 1 gram. Three unique diameters of spherical ZnO nanoparticles were used: 35-45 nm, 80-200 nm, and 500 nm. Ten replicates of each type of specimen were made, five of which were used for compression tests to determine the d_{33} piezoelectric coefficient, and the other five were used for strain tracking tests to determine mechanical properties of the PVDF films.

Once the ZnO particles were added to the solution, the solution was mixed using a vortex mixer and subsequently placed in an ultrasonication bath to break up the ZnO

particles and facilitate dissolution. Samples remained in the ultrasonication bath, being removed and vortexed occasionally, until ZnO particles no longer accumulated at the bottom of the vial, which indicated complete dissolution. The ultrasonication process typically took 1-2 hours depending on the size and mass of ZnO particles in the solution.

Once the ZnO was dissolved, the solution was poured into Petri dishes for solvent casting. The Petri dishes were preheated in the oven at 80 ºC to mitigate the amount of 2-butanone condensation on the inside of the Petri dish cover. If 2-butanone condensed on the inside of the lid, condensate would drip in the center of the specimens, creating a higher localized concentration of solvent, which would leave a hole in the specimen upon evaporation. Samples were heated in the oven at 80 ºC until the 2-butanone was fully evaporated, leaving a PVDF-ZnO thin film, approximately 70 microns in thickness.

To then dissolve the ZnO particles and thus introduce porosity into the thin-films, the PVDF-ZnO specimens were bathed in 10 M HCl (Sigma Aldrich) for 24 hours while continuously stirring with a magnetic stir-bar. The specimens were then removed from HCl and soaked briefly in deionized water to wash off the remaining HCl. Once the samples were dry, they were then ready to be prepared for testing. An example of a finished PVDF film is shown in Figure 7a.

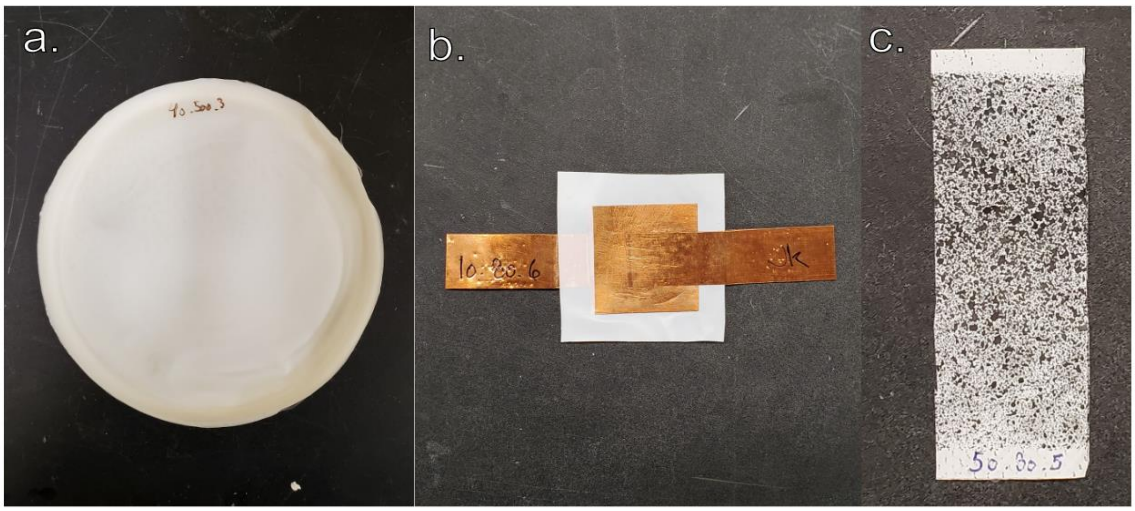

Figure 7: A synthesized PVDF film (a), a specimen prepared for compression testing (b), and a specimen prepared for strain tracking (c)

To estimate the true porosity of the samples, specimens were weighed prior to the HCl bath, and weighed again after a total of 24 hours in HCl. The change in mass of the sample and the initial mass of ZnO added could then be used to estimate the true porosity of the specimens. This calculation is shown in Equation 1:

$$\% \, ZnO \; Removed = \frac{\Delta m}{m_z} \qquad (1)$$

where Δm is the change in mass of the PVDF after ZnO etching, and m_z is the initial mass of ZnO present in the sample before etching.

Since solvent evaporation rate has been shown to have a large effect on the formation of the β-phase conformation of PVDF[28], an experiment was performed to estimate the evaporation rate of the 2-butanone solvent during the solvent casting process of the PVDF films. Five pure PVDF films were fabricated using the methods described above. While the samples were being cast in the oven, they were removed at intervals of 3 minutes and each of their total masses were recorded. After 90 minutes had passed, the

samples were weighed at intervals of 10 minutes (rather than 3 minutes) until all the 2-butanone had evaporated. The change in total mass between each weighing interval was used to calculate the approximate evaporation rate of the 2-butanone in Equation 2:

$$Evaporation\ Rate = \frac{\Delta m}{\Delta t} \quad (2)$$

where Δm is the change in mass of the PVDF film between weighing intervals, and Δt is the change in time between intervals.

Specimens that were meant for compression testing were equipped with 2.5 x 2.5 cm squares of copper tape to act as electrodes, applied to either side of the thin film. The area on the specimen covered by the copper squares was then cut out from the rest of the sample with scissors. Copper tape strips, 1.25 cm in width, were attached to the copper squares to serve as electrical leads, where alligator clips could connect the specimen to a circuit. The other samples, meant for strain tracking, had sections cut out of them in 5 x 2 cm rectangles. These rectangular specimens were then finely speckled with black spray paint so that the speckles could act as positional references on the specimen's surface during the strain tracking process. Examples of specimens prepared for compression testing and strain tracking can be seen in Figure 7b and 7c, respectively.

2.2 Strain Tracking

Once specimens were prepared for strain tracking, they underwent tensile testing. Tensile tests were performed using Newton software from Test Resources and a Test Resources tensile testing instrument (1000 lb_f Actuator). Samples were preloaded to a load of 1 lb_f at a positionally-controlled rate of 0.05 in/s. The preload was sustained for a half second before the major load was applied. The major load ramped up at a rate of 1 lb_f/s to a total applied force of 5 lb_f. During tensile testing, the samples were filmed with

a video camera (image shown in Figure 8a). The load and position data from the tester were recorded using National Instruments data acquisition hardware (NI 9215), and LabVIEW software. Data was collected for the test over a window of 10 seconds at a sampling rate of 1000 Hz.

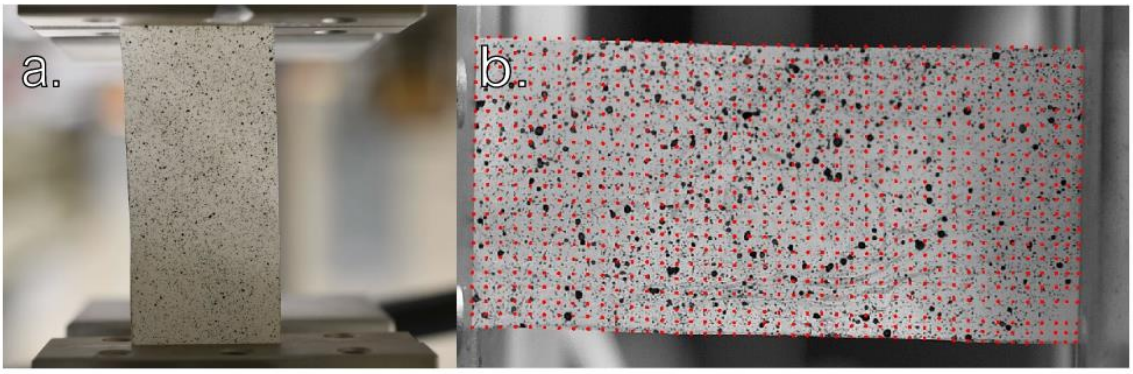

Figure 8: A strain tracking specimen undergoing tensile testing (a), and a specimen with strain tracking nodes overlaying its image (b)

The video recordings of the tensile tests were then processed to determine the strain within the specimen. Using a custom MATLAB code[32], each video was segmented into a series of 21 images over a 10-second window of footage that captured the test, thus, each frame represented a ½-second interval. Once the footage was segmented, a mesh was applied to the first image of the series using Abaqus software. To mesh the image, a 2-D planar part was created in Abaqus which was modeled by tracing the image of the specimen. The part was then meshed using a global element size of 2.5, which typically resulted in approximately 700-1000 elements in the surface mesh. Once the mesh was applied, the data could be exported to MATLAB, which would convert the mesh intersections into individual nodes. The nodes were then scaled for the image using global coordinates from Abaqus and Gimp software. These nodes represented fixed

points on the specimen's surface, which could then be tracked across each frame based on their positions relative to the surrounding black paint marks. Figure 8b shows the nodes in red, overlaying the image of the strain tracking specimen. Using MATLAB, the change in the positions of each node was used to calculate the approximate displacement and strain throughout the specimen. Once the nodes were tracked across each frame, the data was exported to Tecplot360, where the strain data could be visualized using a strain contour map, an example of which is shown in Figure 9. Based on the strain map, regions of consistent strain (in which there were no abrupt changes in the strain contour lines) were isolated for further analysis. The ratio of y-strain to x-strain for each node within the selected region was then examined throughout each frame to determine the Poisson's ratio of the PVDF material. The Poisson's ratio is represented in Equation 3:

$$\nu = \frac{-\varepsilon_y}{\varepsilon_x} \quad (3)$$

where ν is the Poisson's ratio, ε_y is the y-strain, and ε_x is the x-strain. Additionally, the x-strain data and the load data recorded in LabVIEW were used to calculate the stress-strain curve and elastic modulus. The stress, strain, and elastic modulus can be calculated using Equations 4, 5, and 6, respectively:

$$\sigma = \frac{F}{A} \quad (4)$$

$$\varepsilon = \frac{\Delta l}{l_0} \quad (5)$$

$$E = \frac{\sigma}{\varepsilon} \quad (6)$$

where σ is the stress, F is the applied tensile load, A is the cross-sectional area of the specimen, ε is the strain, Δl is the change in length, l_0 is the initial length of the specimen, and E is the elastic modulus.

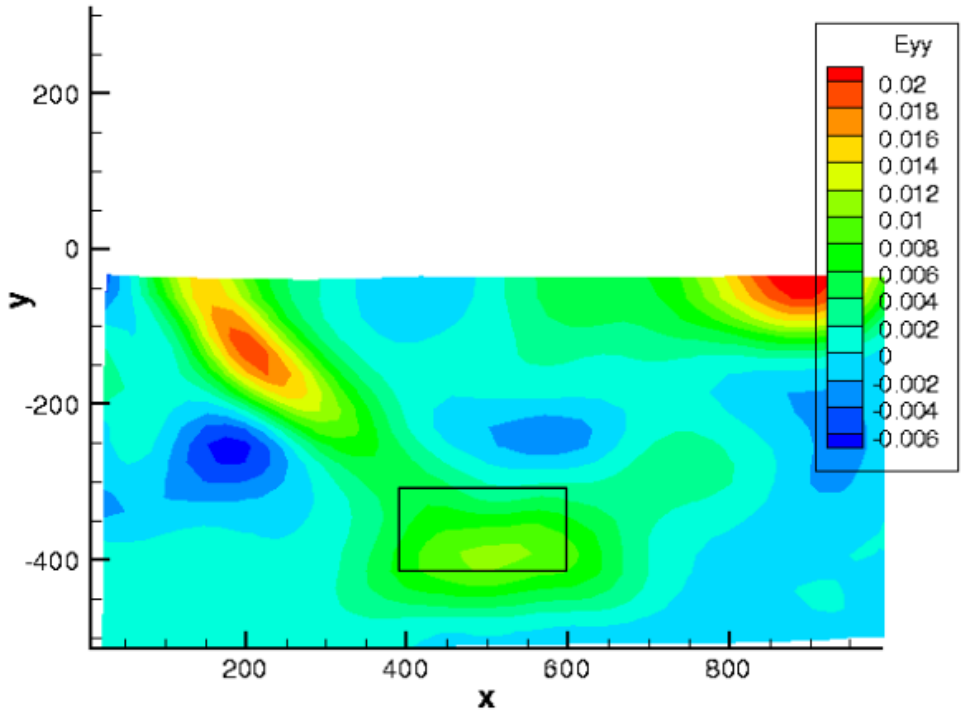

Figure 9: A strain contour map with a region of consistent strain noted with a rectangle

2.3 FEA Simulations

FEA simulations were performed using COMSOL Multiphysics software, specifically using the Piezoelectric Effect Multiphysics tool. A geometric model of a 2.54 x 2.54 cm film with a thickness of 70 microns was built. Domain partitions were created at an offset of 6.35 mm from either end of the film. The material applied to the model was the default PVDF from the COMSOL materials library. To replicate the material properties of the synthesized PVDF films, the elasticity matrix of the material was modified using the elastic moduli and Poisson's ratios determined by the various strain tracking results. The elasticity matrix is shown in Equation 7:

$$D = \frac{E}{(1+\nu)(1-2\nu)} \begin{bmatrix} 1-\nu & \nu & \nu & 0 & 0 & 0 \\ \nu & 1-\nu & \nu & 0 & 0 & 0 \\ \nu & \nu & 1-\nu & 0 & 0 & 0 \\ 0 & 0 & 0 & 1-2\nu & 0 & 0 \\ 0 & 0 & 0 & 0 & 1-2\nu & 0 \\ 0 & 0 & 0 & 0 & 0 & 1-2\nu \end{bmatrix} \quad (7)$$

where *D* is the elasticity tensor, *E* is the elastic modulus, and *v* is the Poisson's ratio. A free tetrahedral mesh was applied to the geometry with element sizes ranging from 0.46-2.54 mm. A floating potential was applied to the top face of the film, and the opposite face was grounded. Each of these faces were connected in series with a 100 nF capacitor in a simulated, modified Sawyer-Tower circuit, displayed in Figure 10.

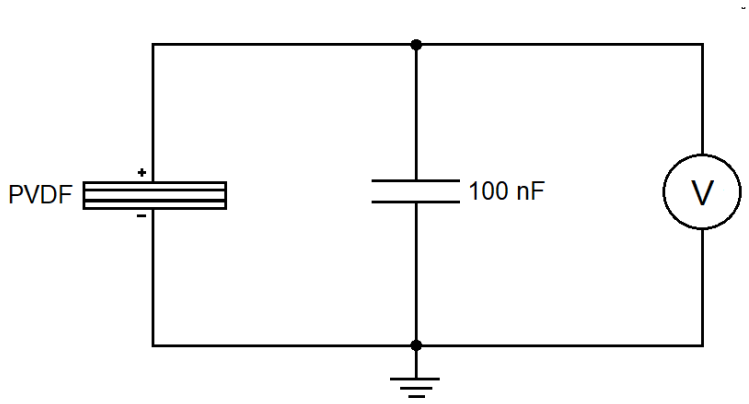

Figure 10: Modified Sawyer-Tower circuit

A simulated compression test was performed to determine the d_{33} piezoelectric coefficient of the PVDF material. This was done by applying a constant, compressive load of 44.48 N to the top surface of the specimen, while applying a fixed constraint to the bottom surface (illustrated in Figure 11). The voltage generated by the simulated specimen under compression across the 100 nF capacitor was used in Equation 8 to calculate the d_{33} coefficient of the material:

$$d_{33} = \frac{Q}{F} = \frac{CV}{F} \quad (8)$$

where d_{33} is the compressive piezoelectric coefficient, Q is the charge in the capacitor, F is the applied compressive load, C is the capacitance of the capacitor, and V is the voltage across the capacitor.

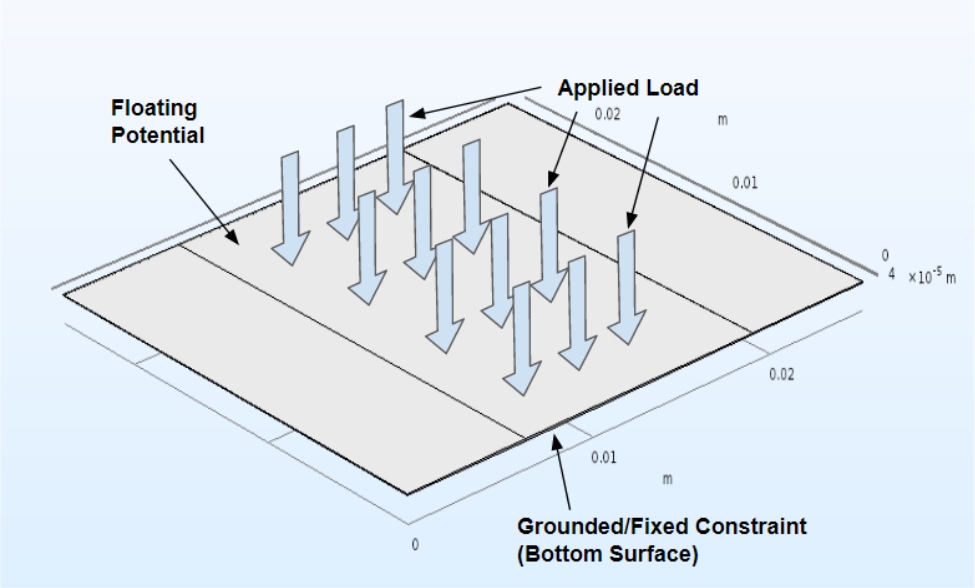

Figure 11: Simulation setup for compression testing

To determine the d_{31} coefficient of the PVDF, simulated tensile tests were performed (illustrated in Figure 12). One of the partitioned bodies was subjected to a ramp load in the transverse direction of 5 N at a rate of 2.5 N/s, while the partitioned body at the opposite end of the film was set with a fixed constraint. Thus, the specimen was loaded in tension. While the modeled specimen underwent mechanical loading, the voltage generated across the 100 nF capacitor was recorded. This voltage, along with the corresponding force applied, were used in Equation 9 to calculate the d_{31} coefficient exhibited by the PVDF film:

$$d_{31} = \frac{Qa}{FA} = \frac{CVa}{FA} \quad (9)$$

where d_{31} is the transverse piezoelectric coefficient, C is the capacitance, V is the voltage across the capacitor, a is the cross-sectional area of the film, F is the applied load, and A is the contact area of the electrode. The simulated d_{33} and d_{31} values were normalized for the total mass of PVDF within the specimen by multiplying by the mass fraction of PVDF in the sample.

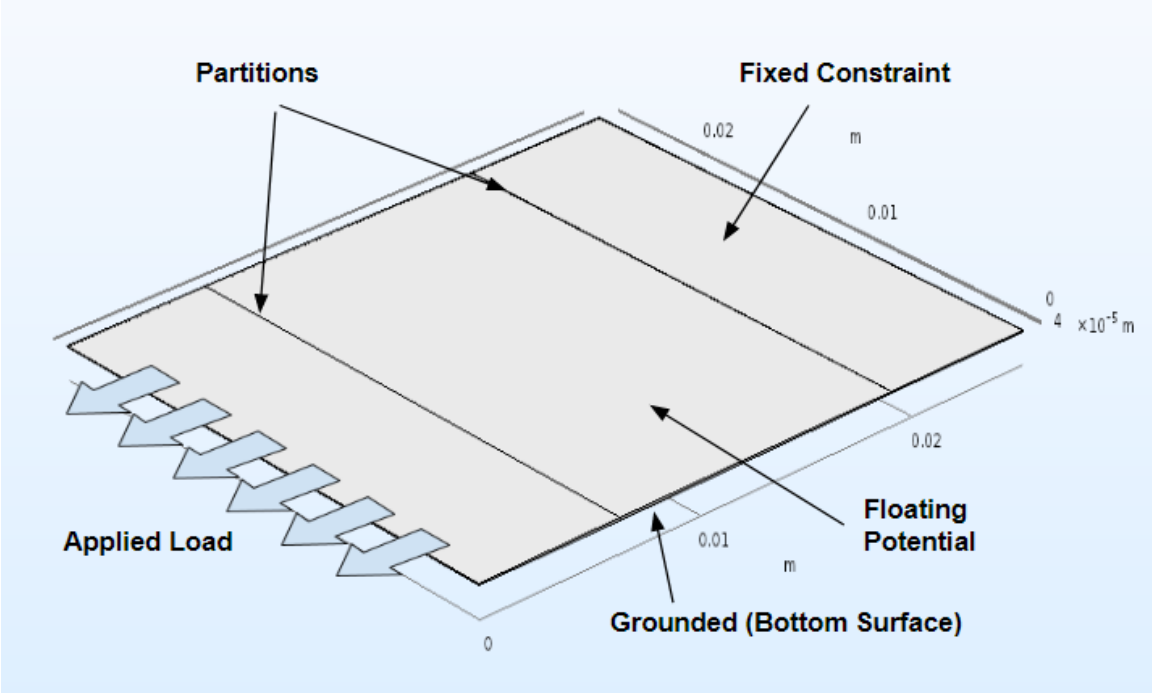

Figure 12: Simulation setup for tensile testing

2.4 d_{33} Compression Tests

Compression tests to determine the d_{33} piezoelectric coefficient of the PVDF were performed by dropping a 200 g cylindrical weight onto the PVDF specimen from a height of 2 cm. This method was used because sharp impact loads were found to produce more clearly discernable peaks in the voltage generated by the PVDF specimens, as opposed to

gradually increasing loads. The specimen was mounted on the lower grips of a tensile tester, with a load cell attached below the grips to measure the impact load of the 200 g weight. The weight was mounted in the upper grips of the tensile tester, and was released during tests by loosening the grip, allowing the cylindrical weight to drop 2 cm onto the PVDF sample below. The electrical leads on the test specimen were connected to either side of a 10 nF capacitor, and the voltage generated by the specimen across the capacitor was measured and recorded in LabVIEW. This experimental setup is shown in Figure 13. Five replicates of each test were taken for each sample.

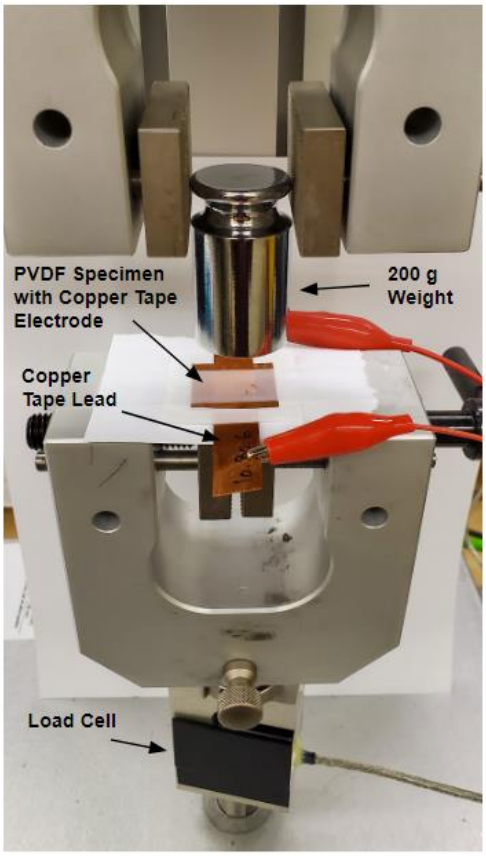

Figure 13: Experimental compression testing setup

The difference between the peak voltage and baseline voltage measured across the 10 nF capacitor in the modified Sawyer-Tower circuit, along with the impact load measured by the load cell, were used in Equation 8 to determine the d_{33} coefficient of the specimen. The signal noise was smoothed using a three-point Savitzky-Golay filter[33], and an example of a signal generated by this method is displayed in Figure 14.

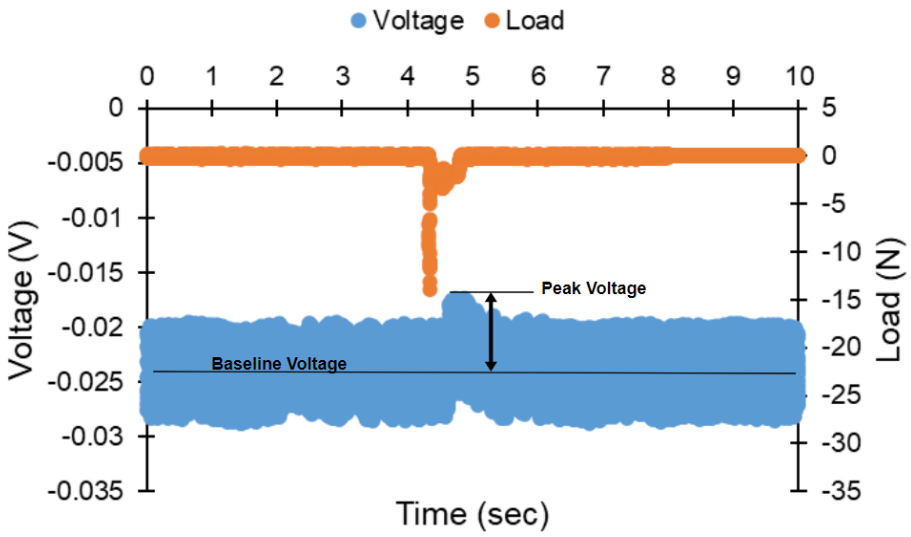

Figure 14: Example of a signal generated across a capacitor by a PVDF specimen during compression

2.5 d_{31} Comparison with Previous Work

The simulated d_{31} results were compared with experimental d_{31} results produced by a previous study from Gao et al[34]. The PVDF films from that study were synthesized using comparable fabrication methods to those used in this study. 35-45 nm ZnO particles were used to introduce porosity into the PVDF films in mass fractions ranging from 10-50% ZnO in increments of 10%. PVDF specimens were loaded under tension, and the voltage generated across the capacitor in a modified Sawyer-Tower circuit was used to determine the d_{31} values.

Chapter 3: Results and Discussion

3.1 Strain Tracking Results

The strain data collected via the strain tracking process, along with the load data collected by LabVIEW during tensile tests, were used to plot stress-strain curves for the PVDF samples. Figure 15 shows examples of stress-strain curves for specimens fabricated with various mass fractions of ZnO. As the mass fraction of ZnO increased (meaning increased porosity), the slope of the stress-strain curve decreased, and the material began to yield at lower stresses. This implies a lower elastic modulus, as well as a lower ultimate tensile strength of the material.

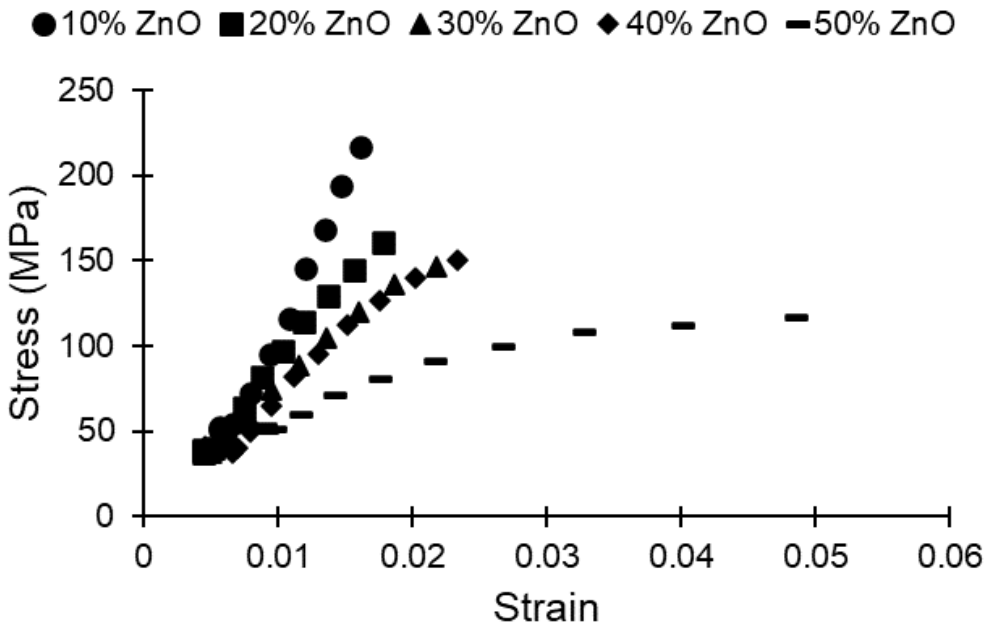

Figure 15: Examples of stress-strain curves for PVDF specimens

Figure 16 displays the mean elastic modulus for each group of PVDF specimens. Each column represents the mean elastic modulus of five identically fabricated specimens, according to their ZnO content and ZnO particle size. The error bars represent plus or minus one standard deviation. Elastic moduli were determined by measuring the slopes of the stress-strain curves in the elastic regions. As the mass fraction of ZnO increased, the elastic modulus of the PVDF was found to decrease ($p<0.01$, using a one-way analysis of variance test). This result confirms expectations that samples with a greater porosity will exhibit more strain under identical stress conditions, which implies that a larger charge separation may be occurring as well. The mean elastic modulus of the pure PVDF specimens was found to be 2.13 GPa. The smallest elastic moduli for each size of ZnO occurred at a mass fraction of 50% ZnO. These smallest elastic moduli values were 0.31 GPa, 0.70 GPa, and 0.60 GPa for the 35-45 nm, 80-200 nm, and 500 nm ZnO specimens, respectively. These represent a reduction in elastic modulus by 86%, 67%, and 72% respectively.

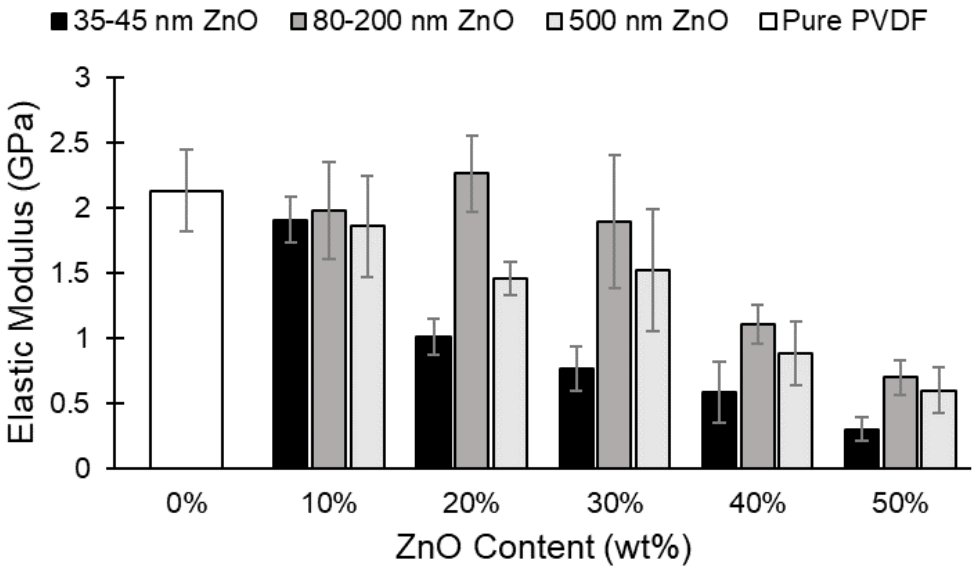

Figure 16: Mean elastic moduli for PVDF specimens of various ZnO content

The PVDF samples made with 35-45 nm ZnO particles exhibited the most rapid falloff in elastic modulus as ZnO content increased, dropping significantly with just 20% ZnO content. The specimens made with 80-200 nm ZnO particles didn't see significant drops in elastic moduli until ZnO content reached 40%, at which point the results fell sharply. The 500 nm ZnO samples showed a more gradual decline in elastic modulus as ZnO content increased, with a noticeable decrease by 20% ZnO, however not as stark a drop as exhibited by the 35-45 nm ZnO samples. A likely reason why the samples made with larger ZnO particles show a less significant decline in elastic modulus is that a smaller fraction of ZnO particles may be removed from the PVDF samples. This could be due to the larger particles taking longer to dissolve in HCl, or possibly that the distribution of the particles in the sample may lead to fewer interactions between the HCl and ZnO.

Figure 17 below shows the weight percent of ZnO removed from the PVDF specimen versus the weight percent of ZnO content added to the specimen. These values were calculated using Equation 1. The data shows that in specimens made with 10-20% ZnO content, only a fraction of the ZnO was removed during the 24-hour HCl bath. In samples with 35-45 nm and 80-200 nm ZnO particles, approximately 50-60% of ZnO mass was removed at these levels, and only 30% of ZnO was removed in samples with 500 nm ZnO particles. In samples with 40-50% ZnO content, however, nearly 100% of ZnO mass was removed for all samples. This disparity in ZnO removal is likely due to ZnO particles being trapped in the PVDF. At lower concentrations of ZnO, a greater amount of ZnO particles will be enveloped by the surrounding PVDF, restricting interaction between the ZnO particles and the HCl. At higher concentrations of ZnO,

more complete pathways form in the material for HCl to permeate, resulting in a greater fraction of ZnO etching.

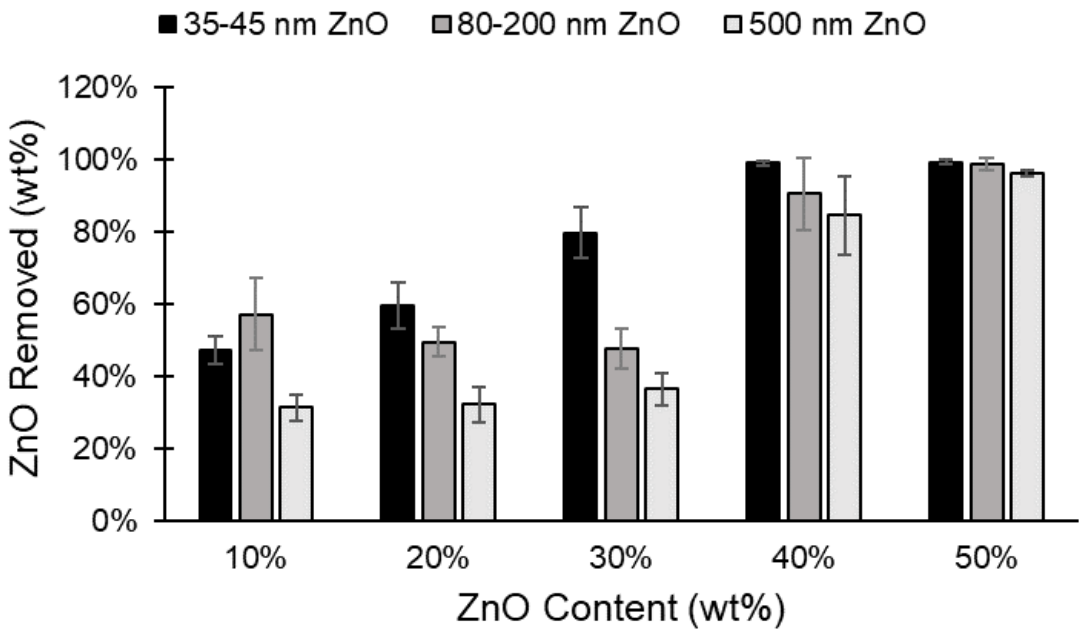

Figure 17: Mean fraction of ZnO removed for PVDF samples of various ZnO content

Another observation that can be made of the ZnO removal data is that the 35-45 nm ZnO particles were removed in greater fractions over the 20%, 30%, and 40% ZnO content samples, while the 500 nm ZnO particles were consistently the least efficiently removed ($p<0.01$). This may be due to the smaller particles dissolving more easily in the HCl, or that the smaller particles may distribute more homogeneously throughout the PVDF, creating more permeation pathways for the HCl. The ZnO removal data is consistent with the elastic modulus data in that the samples with 35-45 nm ZnO particles exhibited an immediate increase in ZnO removal and an immediate decrease in elastic modulus. The samples made with 80-200 nm ZnO particles, however, only exhibited significant changes in ZnO removal and elastic modulus when ZnO content reached 40%. This observation suggests that the amount of ZnO that remains in PVDF samples likely

has a great effect on the elastic modulus of the material, and thus may also affect the piezoelectric performance of the PVDF. One discrepancy in this explanation is that samples with 500 nm ZnO particles exhibited a smaller elastic modulus than those with 80-200 nm ZnO particles, despite having less mass of ZnO removed. This may be due to the effect that the larger size pores have on the elastic modulus of the PVDF. Cabanillas-Casas et al. found that as nano-scale pores in graphene membranes increased in size, the elastic modulus decreased[35]. Therefore, although the number of pores may be fewer, the elastic modulus may be lower in 500 nm ZnO samples due to the increased pore size.

By plotting the y-strain versus the x-strain of a node at various points throughout a tensile test, the slope of the graph can be used to determine the Poisson's ratio.

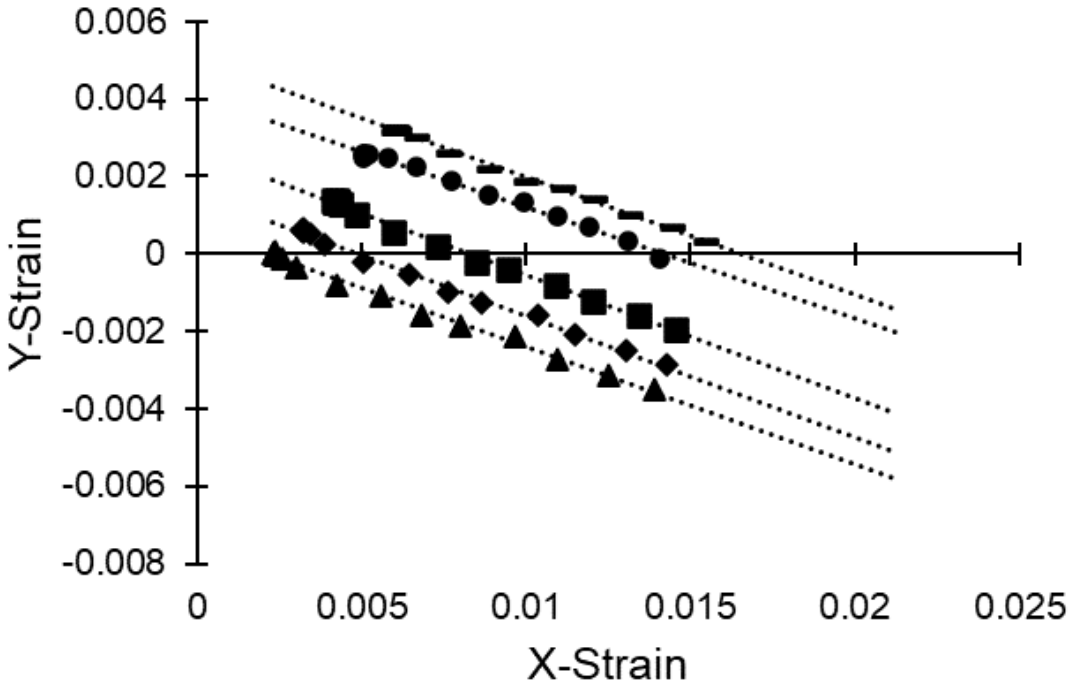

Figure 18: Examples of y-strain versus x-strain plots for various strain tracking nodes during tensile testing

Figure 18 shows examples of y-strain versus x-strain plots for five different nodes at various points during a tensile test. The trendlines estimate the slopes for each of these nodes, which represent the Poisson's ratio exhibited by each node. By taking the mean slope for many of these nodes within a specimen, the overall Poisson's ratio of the material can be estimated. Using this strategy for estimating the Poisson's ratio of the PVDF, the plot shown in Figure 19 was created, which displays the mean Poisson's ratio for each group of five PVDF samples according to their ZnO content and ZnO particle size. The mean Poisson's ratio for the pure PVDF specimens was determined to be 0.32, and the ratio was shown to gradually decline as ZnO content was increased ($p<0.01$). At their lowest, Poisson's ratios of specimens with 50% ZnO reached an average of 0.20, although large standard deviations within the groups of just five samples made it difficult to conclude the true means. There was found to be no statistically significant correlation between ZnO particle size and Poisson's ratio ($p=0.54$).

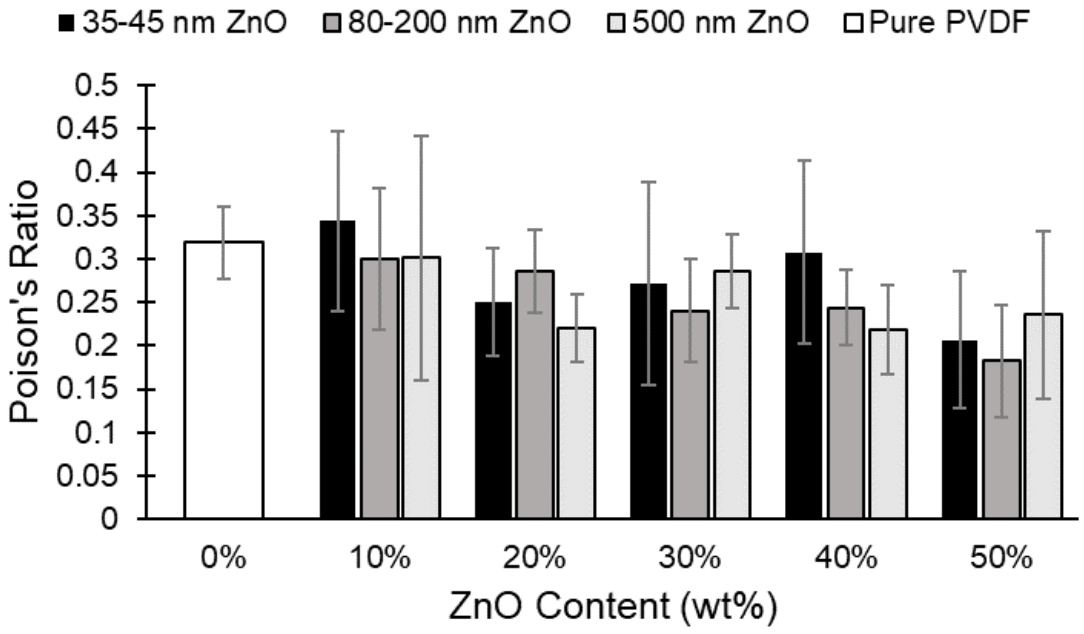

Figure 19: Mean Poisson's ratios for PVDF specimens with various ZnO content

3.2 Simulated d_{33} and d_{31} Results

The elastic modulus and Poisson's ratio values were used to determine the elasticity matrix of the porous PVDF material (Equation 7), and the resulting elasticity matrix was used to edit the PVDF material properties in the COMSOL simulation. Simulations were run to determine the voltage generated across the 100 nF capacitor, and that voltage was used in Equations 8 and 9 to calculate the d_{33} and d_{31} values, respectively. The results of the d_{33} values, normalized for the total mass of PVDF in the samples, are plotted in Figure 20. The simulated pure PVDF films were found to have a mean d_{33} value of 4.8 pC/N, and the greatest d_{33} values in all cases were observed at a ZnO content fraction of 50% ($p<0.01$). At 50% ZnO content, the samples fabricated with 35-45, 80-200, and 500 nm ZnO particle sizes exhibited mean d_{33} coefficients of 16.9, 9.0, and 10.0 pC/N, respectively. These represent increases relative to pure PVDF of 270%, 96%, and 118%, respectively. PVDF specimens made with 35-45 nm ZnO particles exhibited the largest increase in d_{33} at all ZnO content levels of 20% and above. This is consistent with the fact that those 35-45 nm ZnO samples showed the greatest levels of ZnO removal during etching, as well as the smallest elastic moduli. This is in line with the assumption that PVDF with greater porosity will exhibit a smaller elastic modulus and thus undergo greater strain per stress, leading to larger charge separations and higher piezoelectric performance. The samples with 80-200 and 500 nm ZnO particles did not see significant increases in d_{33} coefficients until ZnO content reached 40-50%. Again, this observation correlates with the trend seen in the ZnO removal and elastic modulus findings.

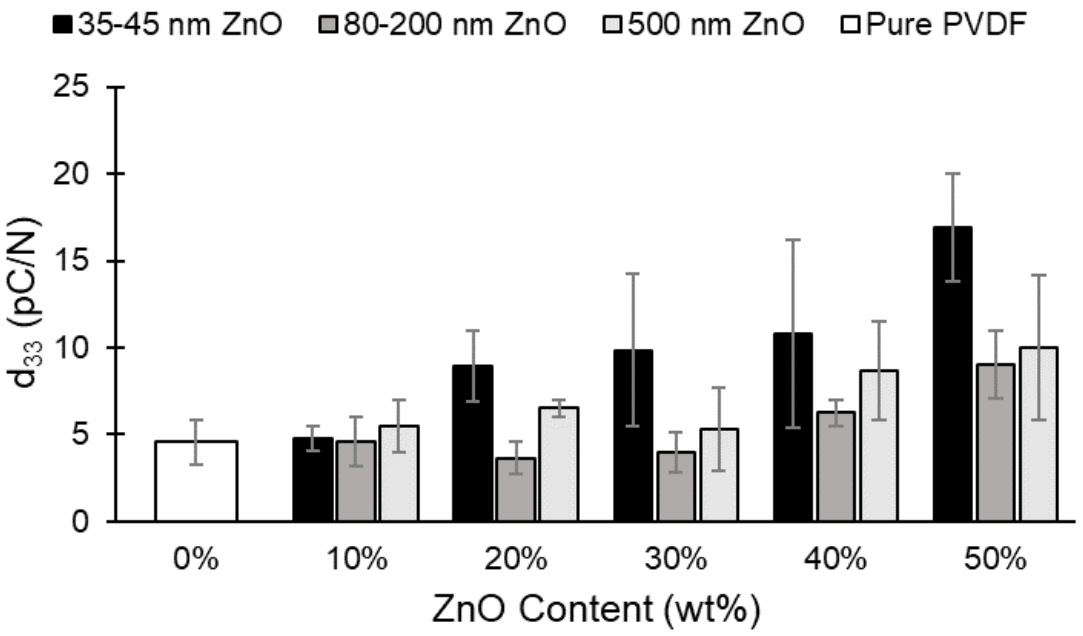

Figure 20: Mean simulated d_{33} values for PVDF with various ZnO content

Similar trends to the d_{33} data were found in the d_{31} coefficient results (Figure 21). The mean simulated d_{31} value for pure PVDF was 16.4 pC/N, and the greatest d_{31} values for each group occurred at 50% ZnO content ($p<0.01$). The greatest mean d_{31} values were 47.2, 21.5, and 29.3 pC/N for samples with 35-45, 80-200, and 500 nm ZnO particles, respectively (increases of 188%, 31%, and 79%, respectively). Again, similar to the d_{33} results, 35-45 nm ZnO samples exhibited significantly increasing d_{31} values at ZnO content levels as low as 20%, whereas d_{31} values for 80-200 and 500 nm ZnO samples did not see an increase in d_{31} until reaching 40-50% ZnO content.

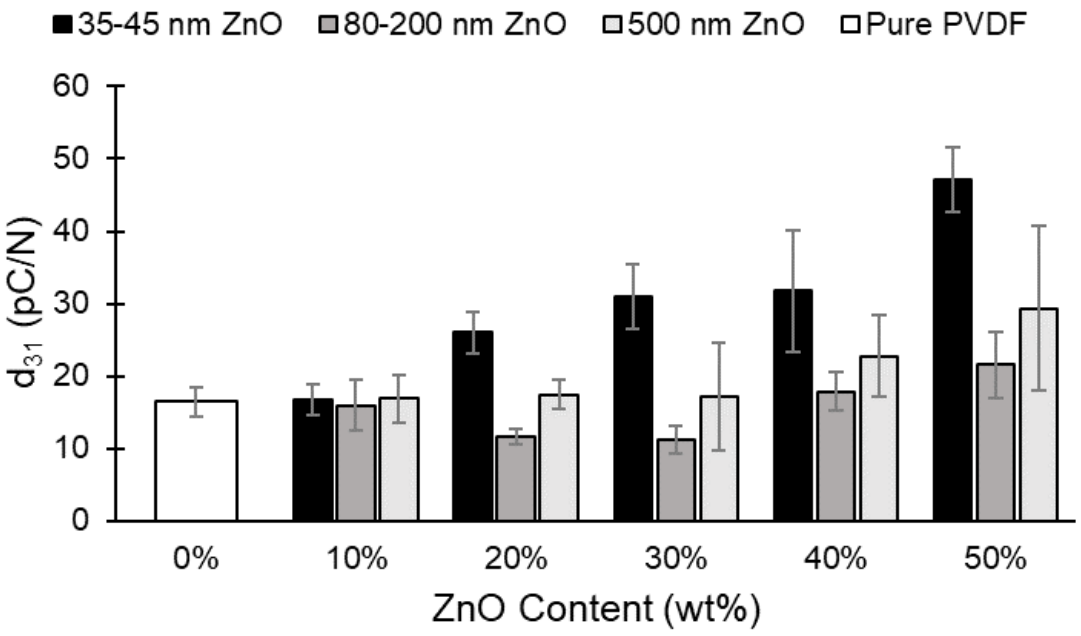

Figure 21: Mean simulated d_{31} values for PVDF with various ZnO content

To further investigate the relationship between the piezoelectric coefficients and the elastic modulus of PVDF, the simulated d_{33} and d_{31} values were plotted against the elastic modulus values in Figures 22a and 22b, respectively. In these plots, a negative logarithmic relationship between the piezoelectric coefficients and the elastic modulus emerges. This relationship is further confirmed by plotting a log-log plot of the same values and observing the linearity of the data (Figures 22c and 22d). The ln(d_{33}) and ln(d_{31}) versus ln(E) plots exhibited R^2 values of 0.78 and 0.84, respectively, with the d_{33} R^2 value being slightly lower due to a few outliers. This data suggests a significant, negative logarithmic relationship between the simulated piezoelectric coefficients and the elastic modulus of the PVDF. A similar plot was made to investigate the relationship between the d_{33}/d_{31} values and the Poisson's ratio, shown in Figure 23a and 23b, respectively. These plots exhibited no discernable trends or relationships between the

Poisson's ratio and the piezoelectric coefficients. This information suggests that the elastic modulus of the PVDF material has a much greater bearing on the overall piezoelectric performance of the material than does the Poisson's ratio.

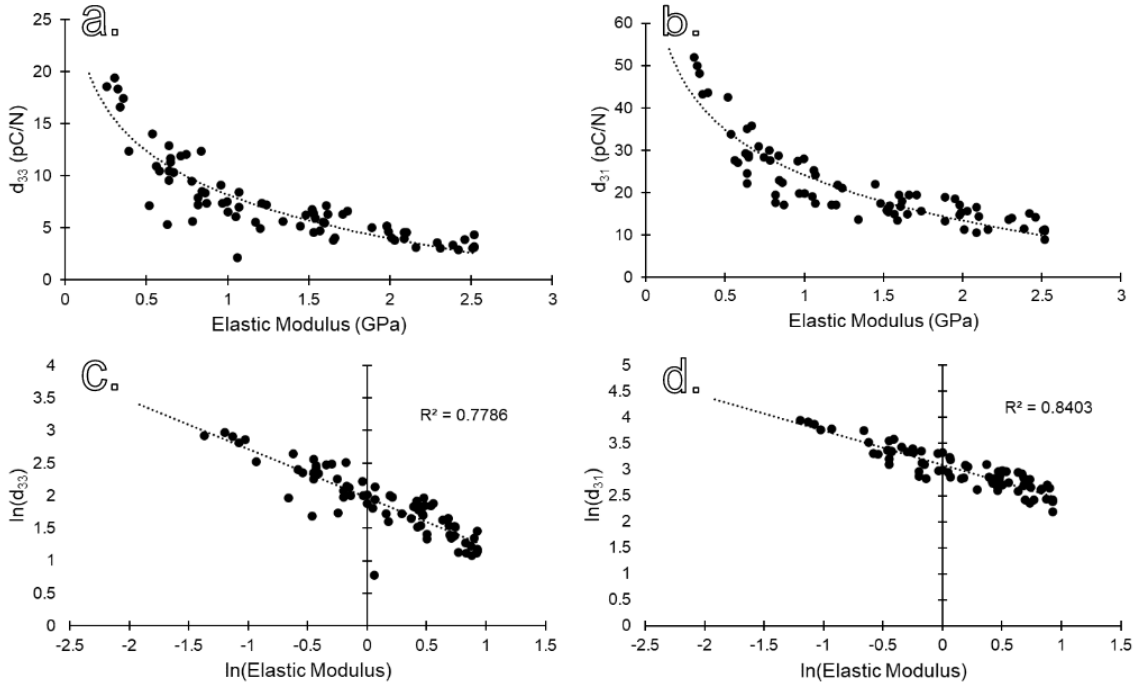

Figure 22: d_{33} and d_{31} versus elastic modulus plots (a and b, respectively) and their log-log plots (c and d, respectively)

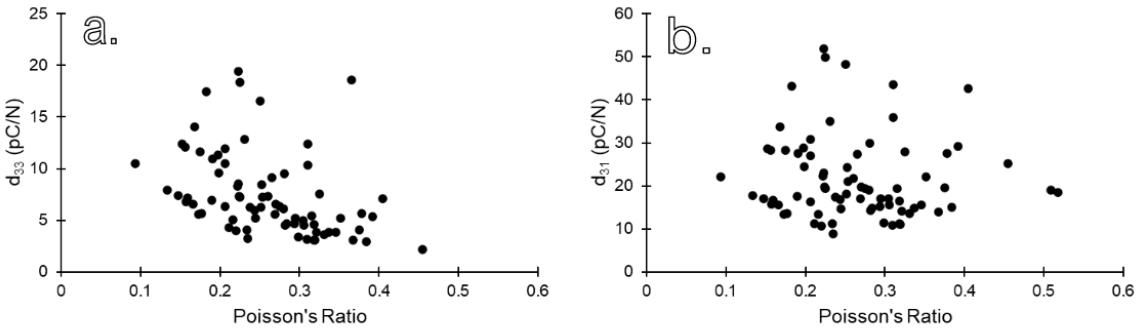

Figure 23: d_{33} and d_{31} versus Poisson's ratio plots (a and b, respectively)

3.3 Experimental Results and Comparisons

Experimental compression tests were performed on the PVDF films to determine their d_{33} piezoelectric coefficients. The voltage generated by the films across a 10 nF capacitor during compression was used in Equation 8 to calculate the d_{33} coefficient of the material. The resulting mean d_{33} values are plotted in Figure 24 according to the ZnO contents and ZnO particle sizes used during the fabrication process for each group of films. The measured mean d_{33} of the pure PVDF samples was 5.1 pC/N. As ZnO content increased, mean d_{33} values ranged between 4-5 pC/N without defining any clear trends. When excluding the pure PVDF specimens, there was no statistically significant difference in d_{33} for samples with varying ZnO content levels (p=0.30).

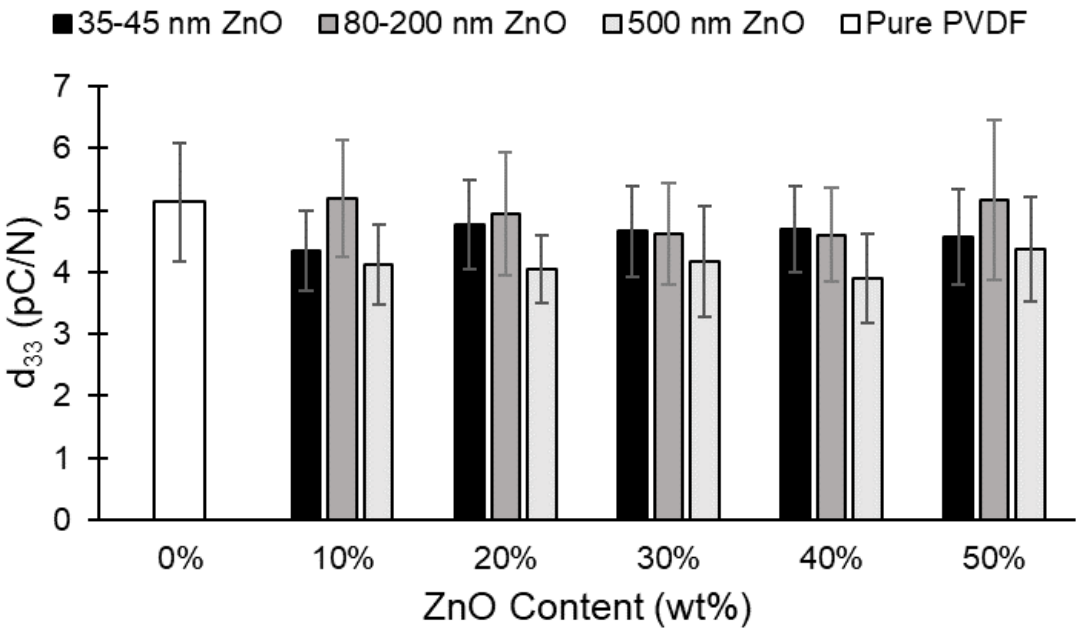

Figure 24: Experimental d_{33} results for PVDF specimens with various ZnO content

There was, however, a significant difference in d_{33} for samples with varying ZnO particle sizes ($P<0.01$), with films fabricated using 500 nm ZnO particles averaging lowest at approximately 4 pC/N, and the 80-200 nm ZnO particle samples averaging the highest in the range of 4.6-5.2 pC/N. These experimental results differ greatly from the expected results based on the FEA simulations. Figure 25a, 25b, and 25c show comparisons between the experimental and simulated d_{33} results for the 35-45, 80-200, and 500 nm samples, respectively.

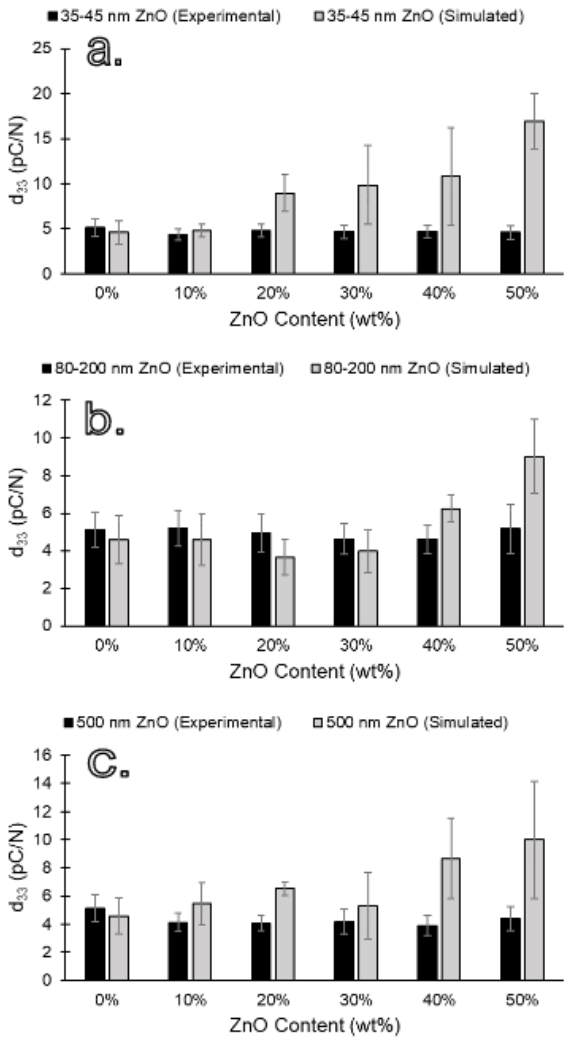

Figure 25: Comparison between experimental and simulated d_{33} results for PVDF synthesized with 35-45 (a), 80-200 (b), and 500 nm ZnO particles (c)

In each case, the d_{33} values were relatively similar for the low ZnO content samples, such as the 0-10% ZnO specimens, averaging around 5 pC/N. However, the experimental d_{33} results did not exhibit the same increase that the simulated results predicted once the ZnO content increased and the elastic modulus decreased.

This disparity in theoretical and experimental results could be attributed to several possible factors. Firstly, ZnO particles remaining in the specimens may act to prohibit charge separations in the PVDF microstructure, and thus dampen signals generated by the material. However, the ZnO removal data (Figure 17) suggests that nearly all ZnO particles were dissolved in HCl when ZnO concentrations reached 40-50%, so it would not be expected that remaining ZnO particles would have an effect on the d_{33} coefficient at those ZnO content levels. A lack of post-synthesis β-phase enhancement techniques may also have contributed to the reduced d_{33} values. Electric poling and mechanical stretching are common techniques for increasing β-phase in PVDF films and improving piezoelectric performance. However, neither of those techniques were utilized in this study, and a lack of β-phase present in the PVDF films may have caused the disparity between the simulated and experimental results. Another possible factor for the lower experimental d_{33} results is that reducing the total mass of PVDF in the films may have a greater negative effect on the d_{33} coefficient than was accounted for in the simulation. That is, as ZnO content increased in the PVDF, the total amount of piezoelectric PVDF material in the films was reduced, which may have affected the voltage output. Although this reduction in PVDF mass was normalized for the simulated d_{33} values by multiplying by the mass fraction of PVDF, the actual effect of reducing PVDF mass may have been greater, leading to the disparity in d_{33} results. Yet another possible cause is that β-phase

concentration in the PVDF films may have been low due to a high solvent evaporation rate during solution casting. Gregorio et al.[28] suggest that the nonpolar α-phase of PVDF begins to form during solution casting when solvent evaporation rates rise above 4.1 mg/min. Figure 26 below shows the measured mean evaporation rate of 2-butanone for five pure PVDF samples fabricated using the methods used for this study. Samples were weighed at intervals of 3 minutes for the first 90 minutes of solution casting in an oven, and then in 10-minute intervals until samples were dry. The differences in weight were used to determine the evaporation rate of the 2-butanone. For the first 90 minutes in the oven, mean evaporation rates ranged from 40-50 mg/min, well above the suggested 4.1 mg/min where α-phase begins to form. Once weighing intervals were changed to 10 minutes, the evaporation rate nearly doubled to approximately 80-90 mg/min, due to the samples remaining in the oven for longer intervals and thus reaching greater temperatures.

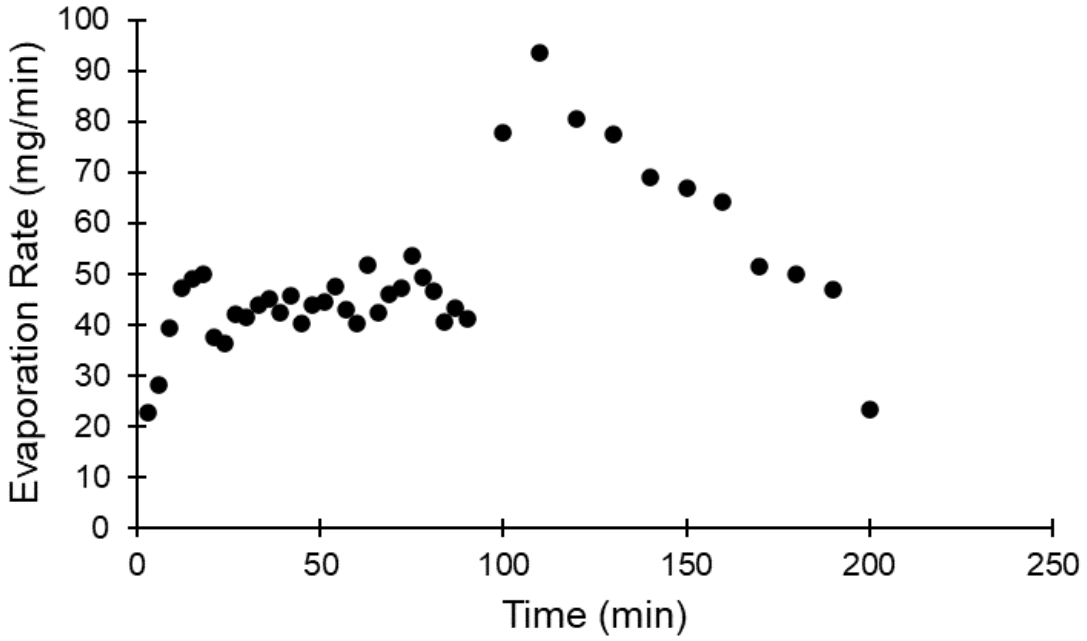

Figure 26: Evaporation rate of 2-butanone during PVDF synthesis

The evaporation rates then began to fall off rapidly as the majority of 2-butanone evaporated. These evaporation rates, which are far greater than those suggested in literature for forming β-phase, may be significantly contributing to a lack of β-phase formation, and thereby hindering the piezoelectric performance of the PVDF films. Finally, it's possible that the d_{33} data collection methods and/or instrumentation were flawed, leading to inaccurate measurements of the d_{33} piezoelectric coefficient. However, a deeper investigation would be necessary to determine whether the methods and instrumentation were reliable.

The elastic modulus and Poisson's ratio data were used to modify the elasticity matrix of the simulated PVDF material for each specimen. Simulated tensile tests were performed to determine the d_{31} piezoelectric coefficient of the PVDF, and the resulting d_{31} values were compared with the experimental d_{31} results achieved by Gao et al.[34] Figure 27 displays the mean simulated d_{31} results for each mass fraction of ZnO (35-45 nm ZnO particles), as well as the mean experimental d_{31} results provided by Gao et al.

For the simulated results, d_{31} increased from 16.7 pC/N to 47.2 pC/N between 10% and 50% ZnO fractions, an increase of 183%. This is compared to the experimental d_{31} results which showed an increase from 21.3 pC/N to 51.3 pC/N, or an increase of 141%. Error between the mean simulated d_{31} and the mean experimental d_{31} values ranged from 7% to 28%. Considering that the average standard deviation for the experimental data was 17%, this data suggests that the simulation used is a reasonably accurate model for estimating the d_{31} of PVDF.

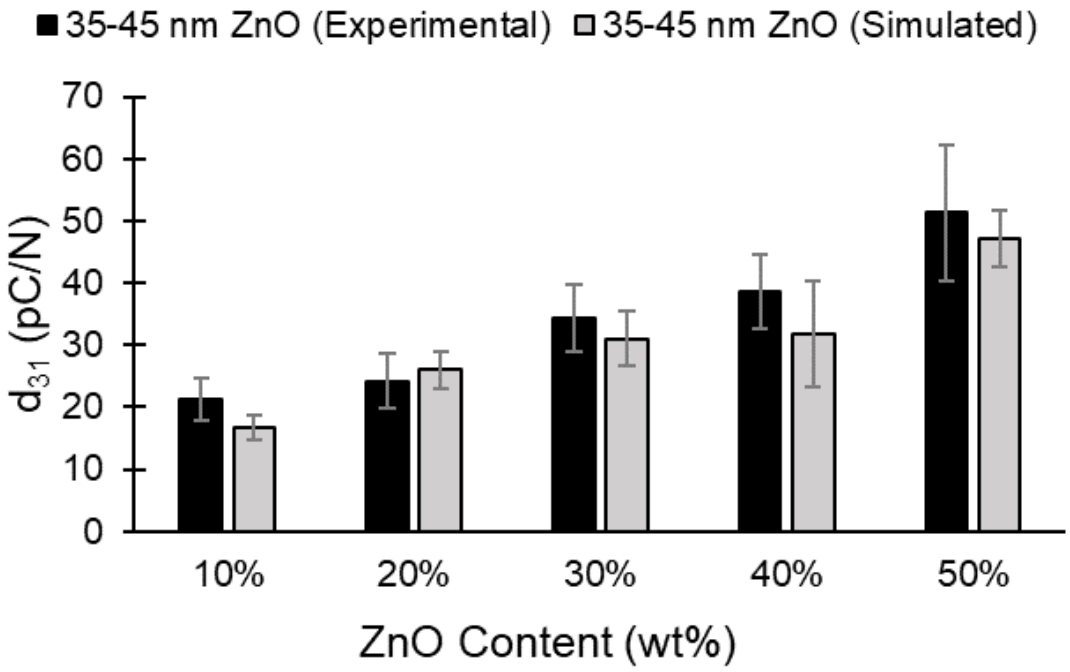

Figure 27: Comparison of simulated and experimental[34] d_{31} results for PVDF specimens of various ZnO content

Chapter 4: Conclusion and Future Work

4.1 Conclusion

The strain tracking method for determining the mechanical properties of the PVDF material revealed that as porosity in the specimens increased (i.e., as ZnO content increased, which was etched away via HCl) the elastic modulus of the material greatly decreased, by as much as 86%. The decline in the elastic modulus was found to be highly inversely correlated with the measured fraction of ZnO removed from the specimens, suggesting that the true porosity was the cause of reduced elastic moduli. In the more porous PVDF films, with lower elastic modulus values, the simulated piezoelectric coefficients d_{33} and d_{31} were found to be significantly greater, increasing by as much as 270% and 188%, respectively, when compared to PVDF with no introduced pores. The elastic modulus was further confirmed to have a negative logarithmic effect on the piezoelectric performance by plotting the natural log of the d_{33} and d_{31} versus the natural log of the elastic moduli and observing the linear trend of the plot. R^2 for $\ln(d_{33})$ and $\ln(d_{31})$ versus $\ln(E)$ were determined to be 0.78 and 0.84, respectively, confirming a significant correlation. Porous PVDF fabricated with 35-45 nm ZnO particles performed the greatest in terms of simulated d_{33} and d_{31}. At 50% ZnO content levels (at which all specimens were highest performing), the samples made with 35-45 nm ZnO particles performed 88% and 69% higher in d_{33} than its 80-200 and 500 nm ZnO counterparts, respectively, and 120% and 61% higher in d_{31} than its 80-200 and 500 nm ZnO counterparts, respectively. These results are consistent with the fact that the 35-45 nm ZnO PVDF specimens exhibited higher rates of ZnO removal, as well as lower elastic modulus values, which may be attributed to more rapid dissolution of smaller ZnO

particles in HCl, or possibly a more uniform distribution of those particles within the PVDF. All these results support the hypothesis that as porosity in PVDF increases, the material undergoes greater strains when subjected to identical mechanical loads, leading to greater charge separations and higher piezoelectric performance.

Strain tracking was also used to determine the Poisson's ratios of the porous PVDF films. It was found that the mean Poisson's ratio decreased as porosity in the films increased. Specimens with no induced pores exhibited a mean Poisson's ratio of 0.32, and the specimens with the greatest porosity (50% ZnO content) exhibited a mean Poisson's ratio of 0.20, a decrease of 38%. The ZnO particle size was found to have no significant effect on the Poisson's ratio of the material. By plotting the simulated d_{33} and d_{31} coefficients versus the Poisson's ratio of the PVDF, it was determined that the Poisson's ratio had a negligible correlation with the piezoelectric coefficients, implying that the elastic modulus was the greatest contributing factor to piezoelectric performance in the simulations.

The experimental d_{33} values were comparable to the simulated values at low levels of porosity, at approximately 5 pC/N. However, as ZnO content increased, the piezoelectric performance of the experimental specimens did not exhibit the same increase as their simulated counterparts, remaining mostly constant at all levels of ZnO content. There are many possible explanations for this observation. The concentration of β-phase in the PVDF may be low due to the lack of polarity enhancement techniques used in this study, or possibly due to the high evaporation rate of the 2-butanone solvent during synthesis. ZnO particles that remain in the samples even after etching may also be affecting the piezoelectric performance. The reduction in the total mass of PVDF as the

porosity increases could also be a factor. Furthermore, instrumentation and/or the methods used for the d_{33} experiments may have been flawed, yielding inaccurate results.

The simulated d_{31} results compared closely with the experimental d_{31} values obtained in a previous study performed by Gao et al.[34] The similarity between the simulated and experimental results suggests that the methods used for simulating the piezoelectric effects of porous PVDF are reasonably accurate at predicting the piezoelectric coefficients of the material.

Understanding how material properties such as the elastic modulus and Poisson's ratio affect the piezoelectric performance of PVDF films, and how those properties can be controlled by altering the porosity of the material, is crucial for further development of PVDF as a pressure sensing material. By improving the piezoelectric performance of PVDF, more sensitive and reliable pressure sensors can be developed for biomedical applications like hemodynamic monitoring. Advancements in monitoring blood flow in the region surrounding a prosthetic aortic valve has the potential to support technological advancements that will improve patient outcomes and benefit physicians and patients alike.

4.2 Future Work

There are several recommendations for future work based on the research covered in this study. Firstly, the effects of a broader range of ZnO particle sizes and concentrations should be studied to determine if the trends observed in this study continue. With ZnO content levels above 50%, piezoelectric performance may increase due to lower elastic moduli, or it may decrease due to diminishing returns and smaller total masses of PVDF. ZnO particles smaller than the 35-45 nm particles used should be

studied to determine if even smaller particles are more easily etched from the PVDF samples, resulting in lower elastic modulus values. Additionally, ZnO removal rates should be further studied to improve etching in HCl at lower concentrations of ZnO and ensure that all ZnO is being removed. Furthermore, the characteristics of pores and remaining ZnO content should be more closely studied on the microscopic level by examining the specimens under a scanning electron microscope (SEM).

The β-phase concentration within PVDF can be enhanced via electrical poling or mechanical stretching. Further work should be done to study how these enhancement methods would interact with the variables considered in this study when improving piezoelectric performance. Similarly, solvents of various evaporation rates should be used to synthesize the PVDF, so as to examine how solvent evaporation during solution casting affects the β-phase concentration and piezoelectric coefficient of the material. Solvents such as dimethylformamide (DMF) have higher boiling points and would evaporate more slowly, possibly resulting in higher concentrations of β-phase. The concentration of β-phase in the PVDF films could be measured using either Fourier-transform infrared spectroscopy (FTIR) or x-ray diffraction (XRD).

The test methods used for determining the d_{33} piezoelectric coefficient can be improved upon to be made more consistent and reliable. It would also be useful to test for piezoelectric performance of the PVDF films in an environment more comparable to the desired application (e.g., subjected to changing pressures in a flow chamber). Finally, the simulation used for determining the piezoelectric coefficients of PVDF can be made more comprehensive by adjusting for variables other than the elasticity matrix alone (e.g.,

editing the coupling matrix to better suit the PVDF material's true characteristics could be incorporated into the study).

Bibliography

[1] H. Jilaihawi, T. Chakravarty, R.E. Weiss, G.P. Fontana, J. Forrester, R.R. Makkar, Meta-analysis of complications in aortic valve replacement: comparison of Medtronic-Corevalve, Edwards-Sapien and surgical aortic valve replacement, Catheterization and Cardiovascular Interventions 80(1) (2012) 128-138.

[2] M.P. Winter, P. Bartko, F. Hofer, M. Zbiral, A. Burger, B. Ghanim, J. Kastner, I.M. Lang, J. Mascherbauer, C. Hengstenberg, G. Goliasch, Evolution of outcome and complications in TAVR: a meta-analysis of observational and randomized studies, Sci Rep 10 (2020).

[3] C.V. Bourantas, P.W. Serruys, Evolution of transcatheter aortic valve replacement, Circulation Research 114(6) (2014) 1037-1051

[4] How tavr devices work – transcatheter aortic valve replacement (TAVR), www.bostonscientific.com, Retrieved May 9, 2022, from https://www.bostonscientific.com/en-US/patients/about-your-device/tavr-devices/how-tavr-devices-work.html

[5] H. Hatoum, A. Yousefi, S. Lilly, P. Maureira, J. Crestanello, L.P. Dasi, An in vitro evaluation of turbulence after transcatheter aortic valve implantation, The Journal of Thoracic and Cardiovascular Surgery 156(5) (2018) 1837-1848.

[6] C.P. Lau, H.F. Tse, Hemodynamic sensors in heart failure devices, Devices for Cardiac Resynchronization (2008) 253-268.

[7] D. Steinhaus, D.W. Reynolds, F. Gadler, G.N. Kay, M.F. Hess, T. Bennett, Implant experience with an implantable hemodynamic monitor for the management of symptomatic heart failure, Pacing and Clinical Electrophysiology 20(8) (2005) 747-753.

[8] D. Prutchi, Medtronic's Chronicle implantable hemodynamic monitor for heart failure monitoring (2012), www.implantable-device.com, Retrieved May 9, 2022 from www.implantable-device.com/2012/01/03/medtronics-chronicle-implantable-hemodynamic-monitor-for-heart-failure-monitoring/

[9] W.T. Abraham, L. Perl, Implantable hemodynamic monitoring for heart failure patients, Journal of the American College of Cardiology 70(3) (2017) 389-398.

[10] P. Ayyadurai, H. Alkhawam, M. Saad, M.A. Al-Sadawi, N.N. Shah, C.E. Kosmas, T.J. Vittorio, An update on the CardioMEMS pulmonary artery pressure sensor, Therapeutic Advances in Cardiovascular Disease 13 (2019).

[11] B. Bera, M.D. Sarkar, Piezoelectric effect, piezotronics and piezophototronics: a review, Imperial Journal of Interdisciplinary Research 2(11) (2016) 1407-1410.

[12] M. Pohanka, The piezoelectric biosensors: principles and applications, a review, International Journal of Electrochemical Science 12 (2017) 496-506.

[13] J.F. Tressler, S. Alkoy, R.E. Newnham, Piezoelectric sensors and sensor materials, Journal of Electroceramics 2(4) (1998) 257-272.

[14] F. Ejeian, S. Azadi, A. Razmjou, Y. Orooji, A Kottapalli, M.E. Warkiani, M. Asadnia, Design and applications of MEMS flow sensors: a review, Sensors and Actuators A: Physical 295 (2019) 483-502.

[15] T. Sharma, K. Aroom, S. Naik, B. Gill, J.X.J. Zhang, Flexible thin-film PVDF-TrFE based pressure sensor for smart catheter applications, Annals of Biomedical Engineering 41 (2013) 744-751.

[16] F. Wang, M. Tanaka, S. Chonan, Development of a PVDF piezopolymer sensor for

unconstrained in-sleep cardiorespiratory monitoring, Journal of Intelligent Material Systems and Structures 14(3) (2003) 185-190.
[17] S. Choi, Z. Jiang, A novel wearable sensor device with conductive fabric and PVDF film for monitoring cardiorespiratory signals, Sensors and Actuators A: Physical 128(2) (2006) 317-326.
[18] Q. Li, J. Xing, D. Shang, Y. Wang, A flow velocity measurement method based on a PVDF piezoelectric sensor, Sensors 19(7) (2019) 1657.
[19] J. G. Rocha, G. Minas, V. Sencadas, S. Lanceros-Mendez, Liquid flow sensor based on PVDF in its beta phase, IEEE International Symposium on Industrial Electronics (2007) 2752-2757.
[20] W. Jung, C. Li, D. Kim, C.H. Ahn, A sensing tube with an integrated piezoelectric flow sensor for liver transplantation, Annual International Conference of the IEEE Engineering in Medicine and Biology Society, (2009) 4469-4472.
[21] N. Chahal, M. Drakopoulou, A.M. Gonzalez-Gonzalez, R. Manivarmane, R. Khattar, R. Senior, Resting aortic valve area at normal transaortic flow rate reflects true valve area in suspected low-gradient severe aortic stenosis, Journal of the American College of Cardiology 8(10) (2015) 1133-1139.
[22] H.S. Brown, M. Halliwell, M. Qamar, A.E. Read, J.M. Evans, P.N. Wells, Measurement of normal portal venous blood flow by Doppler ultrasound, Gut 30(4) (1989) 503-509.
[23] I.T. Gabe, J.H. Gault, J. Ross Jr., D.T. Mason, C.J. Mills, J.P. Schillingford, E. Braunwald, Measurement of instantaneous blood flow velocity and pressure in conscious man with a catheter-tip velocity probe, Circulation 40(5) (1969) 603-614.
[24] P. Iranpour, C. Lall, R. Houshyar, M. Helmy, A. Yang, J.I. Choi, G. Ward, S.C. Goodwin, Altered Doppler flow patterns in cirrhosis patients: an overview, Ultrasonography 35(1) (2016) 3-12.
[25] S. Sukumaran, S. Chatbouri, D. Rouxel, E. Tisserand, F. Thiebaud, T.B. Zineb, Recent advances in flexible PVDF based piezoelectric polymer devices for energy harvesting applications, Journal of Intelligent Material Systems and Structures 32(7) (2021) 746-780.
[26] S. Mishra, L. Unnikrishnan, S.K. Nayak, et al., Advances in piezoelectric polymer composites for energy harvesting applications: a systematic review, Macromolecular Materials and Engineering 304(1) (2019).
[27] D.T. Chinaglia, R. Gregorio Jr., J.C. Stefanello, R.A.P. Altafim, W. Wirges, F. Wang, R. Gerhard, Influence of the evaporation rate on the crystalline phases of solution-cast poly(vinylidene fluoride) films, Journal of Applied Polymer Science 116(2) (2009) 785-791.
[28] R. Gregorio Jr., D.S. Borges, Effect of crystallization rate on the formation of the polymorphs of solution cast poly(vinylidene fluoride), Polymer 49(18) (2008) 4009-4016.
[29] D. Chen, T. Sharma, J.X.J. Zhang, Mesoporous surface control of PVDF thin films for enhanced piezoelectric energy generation, Sensors and Actuators A: Physical 216 (2014) 196-201.
[30] E. Fontananova, J. Jansen, A. Cristiano, E. Curcio, E. Drioli, Effect of additives in the casting solution on the formation of PVDF membranes, Desalination 192(1-3) (2006) 190-197.

[31] Y. Mao, P. Zhao, G. McConohy, H. Yang, Y. Tong, X. Wang, Sponge-like piezoelectric polymer films for scalable and integratable nanogenrators and self-powered electronic systems, Advanced Energy Materials 4(7) (2014).
[32] R. Raghupathy, Form and function: generalized anisotropic inverse mechanics for soft tissues, University of Minnesota (2011).
[33] A. Savitzky, M.J.E. Golay, Smoothing and differentiation of data by simplified least squares procedures, Analytical Chemistry 36(8) (1964) 1627-1639.
[34] Z. Gao, M. Danley, J.T. Kloster, V.K. Lai, P. Zhao, Characterization of nanoporous polyvinylidene fluoride (PVDF) sensors under tensile loading, Smart Materials, Adaptive Structures and Intelligent Systems (2021).
[35] C.J. Cabanillas-Casas, G. Cuba-Supanta, J. Rojas-Tapia, C. Rojas-Ayala, Shape and size of the pore on the mechanical properties of nanoporous graphene membranes, Momento 62 (2021) 63-78.

Appendix A: Piezoelectric Coefficient Derivation

The piezoelectric coefficient is defined in Equation 10 below:

$$d = \frac{D}{\sigma} \quad (10)$$

where d is the piezoelectric coefficient, D is the electric displacement, and σ is the mechanical stress. The electric displacement is further defined in Equation 11:

$$D = \frac{Q}{A} \quad (11)$$

where Q is the charge and A is the contact area of the electrode. By combining 10 and 11, Equation 12 can be derived:

$$d = \frac{Q}{\sigma A} \quad (12)$$

The charge, Q, can be represented as the product of the capacitance and the voltage across the capacitor, shown in equation 13:

$$Q = CV \quad (13)$$

where C is the capacitance and V is the voltage across the capacitor. Combining 12 and 13 results in Equation 14 below:

$$d = \frac{CV}{\sigma A} \quad (14)$$

The stress, σ, can be further defined in Equation 15:

$$\sigma = \frac{F}{a} \quad (15)$$

where F is the applied force on the specimen, and a is the cross-sectional area of the specimen. Combining 14 and 15 gives Equation 16:

$$d = \frac{CVa}{FA} \quad (16)$$

which is the expanded definition of the piezoelectric coefficient, *d*. In the case of d_{33}, the cross-sectional area, *a*, and the area of electrode contact, *A*, are the same. Thus, the two values can be negated, allowing Equation 16 to be simplified in Equation 17:

$$d_{33} = \frac{CV}{F} \qquad (17)$$